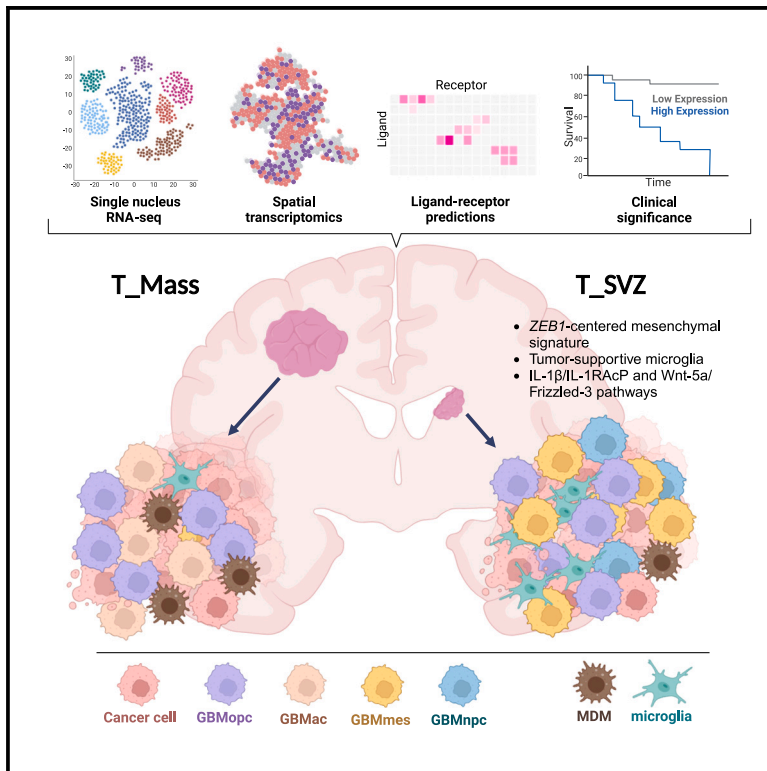# Single-nucleus and spatial landscape of the sub-ventricular zone in human glioblastoma

Graphical abstract

Authors

Yamhilette Licón-Muñoz,
Vanessa Avalos,
Suganya Subramanian, ...,
Muhammad O. Chohan,
Christian A. Bowers, Sara G.M. Piccirillo

Correspondence

spiccirillo@salud.unm.edu

In brief

Licón-Muñoz et al. built a single-nucleus RNA-sequencing-based microenvironment landscape of the tumor mass and the sub-ventricular zone (SVZ) of 15 patients with GBM. They identify a mesenchymal signature and tumor-supportive microglia that establish cell-to-cell interactions with tumor cells in the SVZ through IL-1β/IL-1RAcP and Wnt-5a/Frizzled-3, representing potential targets for GBM treatment.

Highlights

- The SVZ of patients with GBM is characterized by a *ZEB1*-centered mesenchymal signature

- Microglia of the SVZ represent the majority of TAMs and spatially coexist with tumor cells

- Microglia interact with tumor cells in the SVZ through IL-1β/IL-1RAcP and Wnt-5a/Frizzled-3

- IL-1β/IL-1RAcP and Wnt-5a/Frizzled-3 represent potential therapeutic targets in the SVZ

Article

Single-nucleus and spatial landscape of the sub-ventricular zone in human glioblastoma

Yamhilette Licón-Muñoz,[1,2,9] Vanessa Avalos,[1,2,8,9] Suganya Subramanian,[3,4] Bryan Granger,[3,4] Frank Martinez,[1,2] Leopoldo A. García-Montaño,[1,2] Samantha Varela,[5] Drew Moore,[3,4] Eddie Perkins,[6] Michael Kogan,[7] Stefano Berto,[3,4] Muhammad O. Chohan,[6] Christian A. Bowers,[7] and Sara G.M. Piccirillo[1,2,10,*]

[1]The Brain Tumor Translational Laboratory, Department of Cell Biology and Physiology, University of New Mexico Health Sciences Center, Albuquerque, NM 87131, USA
[2]University of New Mexico Comprehensive Cancer Center, Albuquerque, NM 87131, USA
[3]Bioinformatics Core, Department of Neuroscience, Medical University of South Carolina, Charleston, SC 29425, USA
[4]Neurogenomics Laboratory, Department of Neuroscience, Medical University of South Carolina, Charleston, SC 29425, USA
[5]University of New Mexico School of Medicine, Albuquerque, NM 87131, USA
[6]Department of Neurosurgery, University of Mississippi Medical Center, Jackson, MS 39216, USA
[7]Department of Neurosurgery, University of New Mexico Hospital, Albuquerque, NM 87131, USA
[8]Present address: Winship Cancer Institute, Department of Hematology and Oncology, Emory University Laney Graduate School, Atlanta, GA30322, USA
[9]These authors contributed equally
[10]Lead contact
*Correspondence: spiccirillo@salud.unm.edu
https://doi.org/10.1016/j.celrep.2024.115149

SUMMARY

The sub-ventricular zone (SVZ) is the most well-characterized neurogenic area in the mammalian brain. We previously showed that in 65% of patients with glioblastoma (GBM), the SVZ is a reservoir of cancer stem-like cells that contribute to treatment resistance and the emergence of recurrence. Here, we build a single-nucleus RNA-sequencing-based microenvironment landscape of the tumor mass and the SVZ of 15 patients and two histologically normal SVZ samples as controls. We identify a *ZEB1*-centered mesenchymal signature in the tumor cells of the SVZ. Moreover, the SVZ microenvironment is characterized by tumor-supportive microglia, which spatially coexist and establish crosstalks with tumor cells. Last, differential gene expression analyses, predictions of ligand-receptor and incoming/outgoing interactions, and functional assays reveal that the interleukin (IL)-1β/IL-1RAcP and Wnt-5a/Frizzled-3 pathways represent potential therapeutic targets in the SVZ. Our data provide insights into the biology of the SVZ in patients with GBM and identify potential targets of this microenvironment.

INTRODUCTION

Glioblastoma (GBM) is a fatal disease of the adult central nervous system. Poor survival and extensive heterogeneity leading to treatment resistance and emergence of the recurrent tumor are key clinical and biological features. Clinical management of GBM is challenging due to its heterogeneous nature, invasive potential, and poor response to radio- and chemotherapy.[1,2] As a result, GBM inevitably recurs[2] and only 6.9% of patients survive 5 years post-diagnosis.[3] We previously showed that in most patients with GBM, the sub-ventricular zone (SVZ) of the lateral ventricles is a reservoir of cancer stem-like cells (CSCs) that show distinct patterns of treatment resistance compared with matched CSCs from the tumor mass, and contribute to seeding of the recurrent tumor.[4,5] Despite the extensive inter-tumor heterogeneity within GBM, in nearly 80% of patients, the SVZ classifies as the molecular subtype with the worst prog-

nosis,[4] characterized by the presence of tumor-associated macrophages (TAMs),[6–28] which consist of monocyte-derived macrophages (MDMs) and microglia. Therefore, identifying therapeutic targets in the SVZ is key to developing more effective treatments. However, sampling and characterization of the SVZ in GBM is challenging, as this area is extremely small and must be objectively identified during tumor surgical resection.

Given the cellular and molecular intra-tumor heterogeneity characteristic of GBM, the functional role of tumor, and normal cells in the SVZ cannot be predicted based on analyses of samples from the tumor mass. To overcome this challenge, using our fluorescence-guided multiple sampling (FGMS) scheme,[29] we built a single-nucleus RNA-sequencing (snRNA-seq)-based microenvironment landscape of the SVZ (T_SVZ) using tissues from 15 patients with GBM (14 IDH wild-type, 1 IDH mutant). For 14 of these patients, we circumvented the limitations of single-cell RNA-seq by using snRNA-seq, which allowed us to

include frozen samples and preserve the cell composition in the tumor microenvironment. By systematically comparing the T_SVZ with tumor mass (T_Mass) samples isolated from the same patients and two histologically normal SVZ (N_SVZ) samples, and using a number of computational tools and experimental methods, we identified two pathways that represent potential targets in the T_SVZ microenvironment.

RESULTS

A single-nucleus landscape of the tumor mass, tumor SVZ, and normal SVZ microenvironments in patients with GBM

Using our FGMS scheme,[29] we built a single-nucleus landscape of the T_Mass, T_SVZ, and N_SVZ microenvironments in GBM. We collected 15 T_Mass samples and 15 matched T_SVZ samples from 15 untreated patients undergoing surgical resection for presumed high-grade glioma (Table S1A summarizes patient clinical and molecular information). For each sample, we defined the status of the GBM genetic drivers[30,31] (Table S1B). As controls, 2 N_SVZ samples were collected from two individuals: one SVZ was collected postmortem and the other during tumor surgical resection. We performed snRNA-seq using gel bead-in-emulsion technology. We obtained 6.3×10^6 nuclei from T_Mass samples, 8.0×10^6 nuclei from T_SVZ samples, and 1.1×10^6 nuclei from N_SVZ samples (Figure 1A; Table S1C). For each patient and each area (T_Mass, T_SVZ, and N_SVZ), we determined the number of detected genes and unique molecular identifiers (Figure S1A). We sequenced about 3 to 7 × 10^3 nuclei/sample. An estimated total of 59,967, 30,223, and 7,534 cells were detected after sequencing for T_Mass, T_SVZ, and N_SVZ, respectively (Figure 1A). Our pipeline included cell type annotation to define the T_Mass, T_SVZ, and N_SVZ landscapes and subsequent bioinformatic analyses and experimental work to identify transcription factor regulatory networks, define cellular dynamics, identify differentially expressed genes of the three areas, and characterize TAMs. These steps were followed by spatial transcriptomics, ligand-receptor predictions, and functional phenotyping to identify interactions specific to the T_SVZ and define their clinical significance (Figure 1A). We integrated data from all patients by areas (T_Mass, T_SVZ, and N_SVZ, Figure 1B top left), and by cluster (Figure 1B top right) and calculated the proportion of cells in the three areas for each patient by cluster (Figures 1C and S1B). Of note, cluster 15 was exclusive to the two N_SVZ samples (histologically normal samples 1 and 2, HNS1 and 2), confirming that these two samples were distinguishable from the T_Mass and T_SVZ (Figures 1C and S1B).

Transcriptional analysis of copy-number variations (CNVs) by inferCNV[32] was used to find alterations (amplifications and deletions) in each cluster of the T_Mass and the T_SVZ having the N_SVZ clusters as a reference. We first integrated data (Figure 1D top), and then calculated the proportion of tumor and normal cells by clusters (Figure 1D bottom). We confirmed that the N_SVZ was composed of normal cells only and had a normal chromosomal landscape (Figure S2) and identified expected CNVs such as chromosome 7 amplification and chromosome 10 deletion in the T_SVZ (Figure 1E) and the T_Mass (Figure S2).

For each cell subset identified by clustering in each area, we annotated cell types based on known markers and reference classifiers (Figure 1F top; Figure S3A). Tumor cells depicted in Figure 1F were assigned using the cell state classification by Neftel et al.[16] We also calculated the proportion of each cell type in the three areas (Figure 1F bottom). Among the tumor cell states, the astrocyte-like (GBMac) state was not represented in the T_SVZ (Figure 1F bottom middle), while tumor cells in matched T-Mass samples represent all four cell states: GBMac, oligodendrocyte-progenitor-like (GBMopc), mesenchymal-like (GBMmes), and neural-progenitor-like (GBMnpc) (Figure 1F bottom left). GBMopc and GBMac were present in similar proportion in the T_Mass (17.4% and 17.2%, respectively) and were the most abundant tumor cell populations in this area, while GBMmes was the second most abundant state in the T_SVZ (13.2% vs. 6.5% in the T_Mass). The T_SVZ also showed an increase in the GBMnpc state (10.1% vs. 5.5% in the T_Mass). Some tumor cell clusters in both areas (22.2% in the T_SVZ and 10.5% in the T_Mass) could not be captured by the existing four states[16]; we labeled those clusters as CancerCell. The same analysis was performed for each patient and each area allowed us to quantify the abundance of each tumor cell state[16] (Figure S3B).

Among TAMs, microglia were more abundant in the T_SVZ compared with MDMs (10.5% vs. 1.7%) (Figure 1F bottom middle), whereas both cell types were similar in the T_Mass (7.6% and 5.5%, respectively) (Figure 1F bottom left). The N_SVZ was composed of the expected normal brain cell types, including oligodendrocytes, astrocytes, and neurons. The correct sampling of the tissue adjacent to the ventricle in the N_SVZ was confirmed by the presence of ependymal cells (Figure 1F bottom right), in agreement with a previous report.[33]

Overall, these results show that the T_SVZ is characterized by a different cellular landscape than the T_Mass and the N_SVZ.

The tumor SVZ microenvironment harbors tumor cell populations characterized by a *ZEB1*-centered mesenchymal signature and a distinct regulon profile of microglia

We started our analysis by defining the cellular dynamics of tumor cells in the T_Mass and the T_SVZ. Using CellRank 2,[34,35] we identified macrostates in the two areas. Macrostates are groups of cells marked by similar gene expression profiles and cellular dynamics. The number of total macrostates is selected heuristically using an elbow graph. Macrostates are mapped to specific cell classes or other annotations according to their overlap using underlying gene expression; thus, multiple macrostates may align with the same cell class. In this analysis, we found that the T_Mass was characterized by three GBMac macrostates (GBMac p1, p2, and p3), one GBMopc, one GBMnpc, and one GBMmes (Figure 2A left). In contrast, the T_SVZ was characterized by three GBMmes macrostates (GBMmes p1, p2, and p3), two CancerCell (CancerCell p1, and p2), and one GBMopc (Figure 2A right). CancerCell and GBMmes cells were more undifferentiated than other tumor cells in the T_Mass and in the T_SVZ, respectively, suggesting different transcriptional dynamics and directional flows among cell populations (Figure 2A). We then identified initial and terminal states
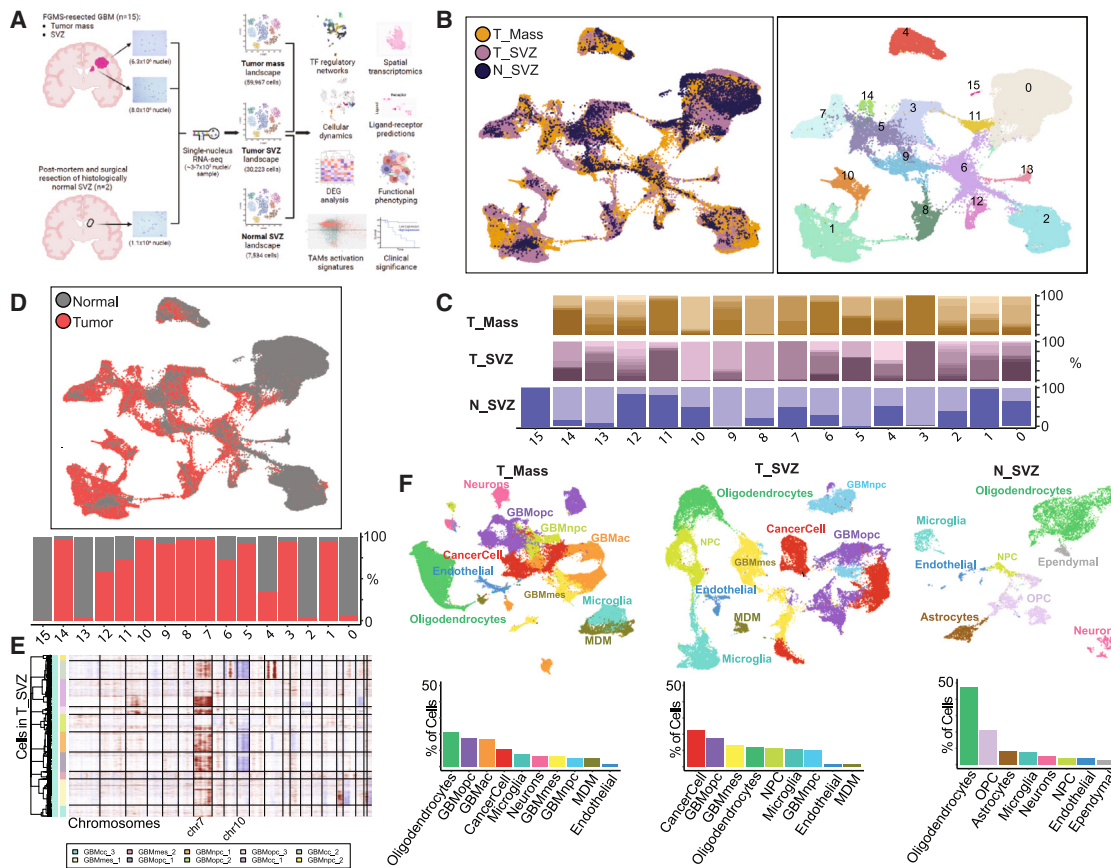
Figure 1. A single-nucleus landscape of the tumor mass, tumor SVZ, and normal SVZ microenvironments in patients with GBM

(A) Schematic of the tissue collection pipeline using our previously published fluorescence-guided multiple sampling (FGMS) scheme.[29] Tumor mass and SVZ samples were collected from 15 patients. Histologically normal SVZ samples were collected from two individuals: one SVZ was collected as postmortem tissue and the other during tumor surgical resection. Due to poor sample quality, cells obtained from GBM4 are not included in the counting shown in this schematic. The number of cells obtained from each area, based on the number of total nuclei sequenced, is in parentheses under each illustrative Uniform Manifold Approximation and Projection (UMAP). Bioinformatic analysis and experimental work were performed to identify the transcription factor (TF) regulatory networks, define cellular dynamics, identify differentially expressed genes (DEGs) and tumor-associated macrophage (TAM) activation signatures, followed by spatial transcriptomics analysis, ligand-receptor predictions, and functional phenotyping to identify interactions specific of the tumor SVZ with clinical significance. Created with BioRender.com.

(B) Integrated UMAPs of all cells by area (Tumor Mass = T_Mass, yellow; Tumor SVZ = T_SVZ, purple; Normal SVZ = N_SVZ, blue) (left) and cluster (right).

(C) Proportion of cells in the three areas from each patient by cluster (same color code as in B). The gradient color indicates the patient contribution to the identified clusters in each area.

(D) Integrated UMAP of all cells colored by class (normal = gray and tumor = red based on copy-number variations, top) and proportion of cells from each class by cluster (bottom).

(E) Copy-number variations in integrated T_SVZ samples and clustered by cancer cell types (y axis). Genomic region of each variation is presented by chromosomal location (x axis). Reference cells are from integrated N_SVZ samples (Figure S2).

(F) UMAPs of each area showing cell type annotation. T_Mass (left), T_SVZ (middle), and N_SVZ (right), top. Proportion of each cell type in the three areas, bottom. Tumor cells were annotated using the cell state classification of Neftel.[16] NPC, neural progenitor cells; OPC, oligodendrocyte precursor cells; MDM, monocyte-derived macrophages.

(Figures 2B and S4A), and fate probabilities (Figure S4B) and asked whether the initial macrostates differed between the two areas. Specifically, in this analysis, the state with the lowest incoming transition probabilities is automatically assigned as an initial state. Conversely, the state(s) with the highest incoming or self-transition probabilities are assigned as terminal states, while all others are deemed intermediate. The initial macrostate of the T_Mass was GBMac p3 (Figure 2B left), whereas for the T_SVZ it was GBMmes p1 (Figure 2B right). Moreover,

latent time analysis revealed additional differences between the T_Mass (Figure 2C left) and the T_SVZ (Figure 2C right) at the level of transcription factors (TFs) and co-factors. Only the T_SVZ had distinct expression patterns: some TFs and co-factors, such as *ANXA11*, *HIF1A*, and *FOXO1*, showed an initial expression trend, whereas others, such as *GLI2* and *ID4*, had a terminal expression trend (Figure 2C right). In contrast, the T_Mass was characterized by TFs and co-factors with terminal and more homogeneous expression trends (Figure 2C left).
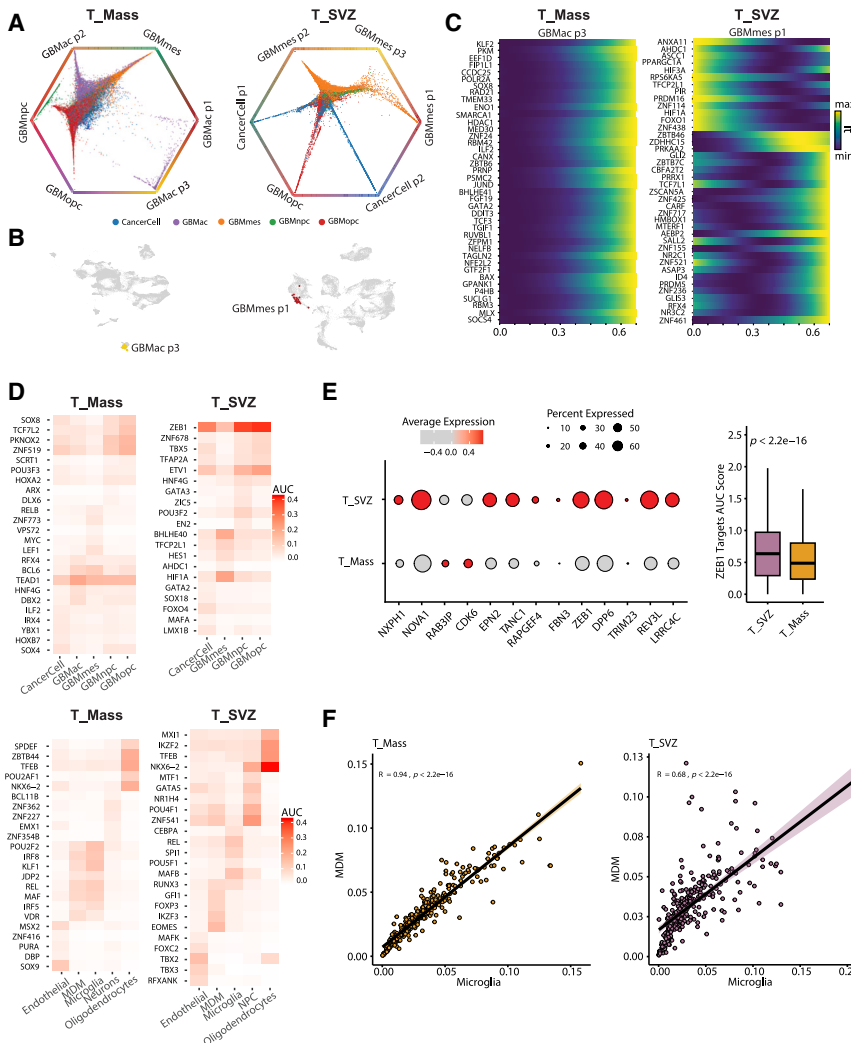
Figure 2. The tumor SVZ microenvironment harbors tumor cell populations characterized by a *ZEB1*-centered mesenchymal signature and a distinct regulon profile of microglia

(A) Circular projections of tumor cells according to fate probabilities toward the macrostates, with cell type annotation as in Figure 1F. Only tumor cells of the T_Mass (top left) and T_SVZ (top right) were analyzed using CellRank 2.[34,35]

(B) CellRank 2-computed initial macrostates in the T_Mass (bottom left) and T_SVZ (bottom right). Macrostates are color-coded as in (A).

(C) Area-specific heatmaps (T_Mass, left and T_SVZ, right) showing gene expression trends of the top 40 genes with expression sorted according to latent time. Only transcription factors and co-factors are shown.

(D) Heatmaps of regulon enrichment expressed as area under the curve (AUC) of all T_Mass and T_SVZ samples. Regulons were identified by single-cell regulatory network inference and clustering (SCENIC).[36,37] Tumor cells of each area (top) and normal cells (bottom) are depicted. Only the top 5 regulons for each cell type are shown. Cell type annotation as in Figure 1F.

(E) Dotplot showing gene expression of SCENIC-identified ZEB1 targets in T_SVZ and T_Mass (left). Boxplot showing AUC module score of SCENIC-identified ZEB1 target genes between T_SVZ and T_Mass. Wilcoxon Rank-Sum test was used to determine significance ($p < 2.2E{-}16$, right).

(F) Pearson's correlation analysis of regulons between monocyte-derived macrophages (MDMs) and microglia in the T_Mass (left) and T_SVZ (right). $p < 2.2E{-}16$ for both correlations.

Given the different cellular dynamics in the tumor cells of the T_SVZ compared with the T_Mass, we then performed single-cell regulatory network inference and clustering (SCENIC)[36,37] of all T_SVZ and T_Mass samples (Figure 2D) and of each individual sample (Figure S5) to identify the key master regulators of the tumor cells in the T_SVZ. While the TF and regulator of cell migration *TEAD1*[38,39] was specific to tumor cells in the T_Mass, especially in the GBMac state (Figure 2D top left), the key mesenchymal TF *ZEB1*[40–42] was exclusively expressed in the T_SVZ, with highest enrichment in the GBMnpc and GBMopc states and lowest in the GBMmes state (Figure 2D top right). This may be because the GBMmes state was defined by genes related to wound healing, inflammatory response, and hypoxia, among others, but not mesenchymal processes, as recently suggested.[43] Moreover, ZEB1 targets are significantly upregulated in the tumor cells of the T_SVZ compared with the tumor cells of the T_Mass (Figure 2E). Other regulons highlighted distinct regulatory networks in the two areas: (1) *ZNF519*, *PKNOX2*, and *TCF7L2* showed enrichment in the GBMopc state of the

T_Mass. Notably, *TCF7L2* is an effector of the Wnt/β-Catenin signaling pathway with prognostic significance in patients with GBM[44] (Figure 2D top left); (2) *ETV1*, *BHLHE40*, and *HIF1A* were enriched in the T_SVZ, with *ETV1* having the highest enrichment in the GBMopc state, whereas *BHLHE40* and *HIF1A* were highest in the GBMmes state, as expected for a state linked to hypoxia genes[16,43] (Figure 2D top right).

We next calculated regulon enrichment in the matched normal cells of the T_Mass and the T_SVZ (Figure 2D bottom). Although MDM and microglia of the T_Mass shared a core set of regulons, including *POU2F2*, *KLF1*, and the regulator of macrophage differentiation *IRF8* (which confers an immunosuppressive phenotype in MDMs[45] and promotes reactivity in microglia[46]), in the T_SVZ, MDM and microglia were characterized by distinct regulons, including *REL* and *MAFB* in microglia and *EOMES* in MDMs (Figure 2D bottom right), suggesting differences in the functional roles of these immune cell populations. To further explore these differences, we performed correlation analyses of regulons in MDMs and microglia in the T_Mass (Figure 2F left) and in the T_SVZ (Figure 2F right). MDM and microglia in the T_SVZ showed a weaker correlation than the same cell populations in the T_Mass (R = 0.68 vs. R = 0.94).
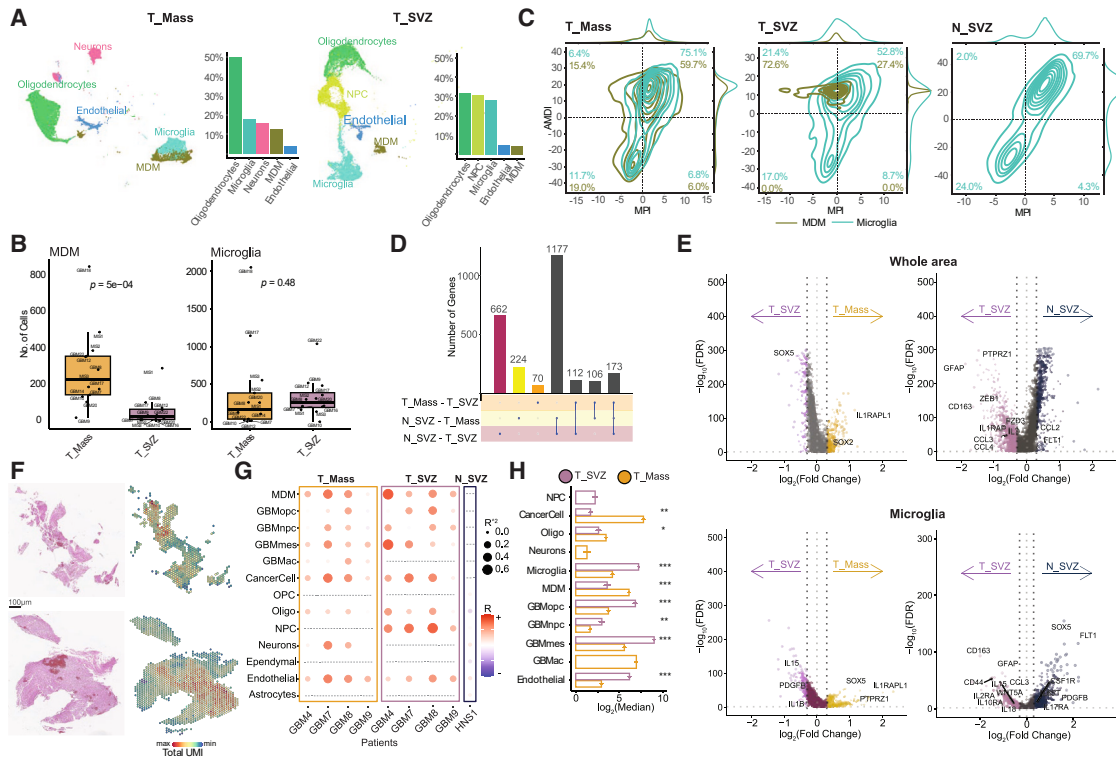
Figure 3. Tumor-supportive microglia are the majority of TAMs in the tumor SVZ microenvironment and spatially coexist with tumor cells

(A) UMAPs of normal cell populations in the T_Mass (left) and T_SVZ (right) with proportion of each cell type in the two areas.

(B) Boxplot depicting TAMs' abundance (monocyte-derived macrophages [MDMs] and microglia) by patient between T_Mass and T_SVZ. Wilcoxon Rank-Sum test was used to determine significance. $p = 5E-04$ (left), $p = 0.48$ (right).

(C) MacSpectrum plots of MDMs (olive green) and Microglia (green) with percentages calculated for each quadrant in the T_Mass (left), T_SVZ (middle), and N_SVZ (right). AMDI, Activation-induced Macrophage Differentiation Index; MPI, Macrophage Polarization Index.

(D) Upset plot depicting the number of differentially expressed genes (DEGs) in the comparisons among T_Mass, T_SVZ, and N_SVZ. The magenta, yellow, and orange bars represent the number of DEGs that are unshared among the comparisons. The gray bars represent the shared DEGs among the indicated comparison.

(E) Volcano plots showing the differentially expressed genes in T_SVZ vs. T_Mass (left) and T_SVZ vs. N_SVZ (right) as whole areas, top. Volcano plots showing the differentially expressed genes in microglia only in T_SVZ vs. T_Mass (left) and T_SVZ vs. N_SVZ (right), bottom. In all analyses, average $\log_2$(Fold Change) > 0.3 and $p < 0.05$ were used.

(F) Representative images of the T_Mass (top) and T_SVZ (bottom) from tissue sections used for spatial transcriptomics. Sections of GBM7 are shown as an example. Images of hematoxylin and eosin-stained tissues (left) and the corresponding digital images (right). Scale bar, 100 μm. Color code = minimum to maximum total unique molecular identifier (UMI) for each sample.

(G) Dot plot of Pearson's spatial correlation between microglia and all other cell types in T_Mass and T_SVZ of four patients. Cell types exhibiting spatial correlation with microglia (y axis). GBM samples, areas and normal sample HNS1 (x axis). The dashed lines indicate the absent cell types.

(H) Bar graph showing patterns of spatial dependencies among cell types in the T_Mass (yellow) and in the T_SVZ (purple) from the same patients as in Figure 3G. All cell types in the two areas were analyzed. Cell types exhibiting spatial dependencies (y axis) and $\log_2$ (median) of total spatial dependencies (x axis). *$p < 0.05$, **$p < 0.01$, ***$p < 0.001$. NPC, neural progenitor cells; OPC, oligodendrocyte precursor cells; MDM, monocyte-derived macrophages.

Overall, these results indicate that the T_SVZ harbors tumor cells characterized by a *ZEB1*-centered mesenchymal signature and a distinct regulon profile of microglia.

Tumor-supportive microglia are the majority of TAMs in the tumor SVZ microenvironment and spatially coexist with tumor cells

Our results above led us to perform functional characterization of microglia. Initially, we visualized only clusters of normal cells of the T_Mass and the T_SVZ and calculated the proportion of each cell type (Figure 3A). This analysis confirmed that MDMs represent the minority of TAMs and the least abundant normal

cell type of the T_SVZ (4.6% of total normal cells), whereas microglia were the third most abundant cell type in this area (28.4% of total normal cells; Figure 3A right). In the T_Mass, microglia and MDMs were present in a more similar proportion (17.7% and 12.8% of total normal cells, respectively; Figure 3A left). Neural progenitor cells (NPCs) represent the second most abundant cell type in the T_SVZ but were absent in the T_Mass microenvironment. Conversely, neurons represent the third most abundant cell type in the T_Mass but were absent in the T_SVZ (Figure 3A).

Intrigued by the data on the proportion of each cell type in the T_SVZ, we observed that the number of MDMs is significantly

reduced in the T_SVZ compared with the T_Mass (Figure 3B left) and that microglia show a trend of increased abundance in the T_SVZ compared with the T_Mass (Figure 3B right). Next, we performed functional characterization of the microglia and MDMs in the T_SVZ compared with matched cell populations in the T_Mass. Although M1 is typically synonymous with "proinflammatory/anti-tumor" and M2 with "anti-inflammatory/pro-tumor," these definitions do not fully represent the functional identity of TAMs in GBM. Thus, we used MacSpectrum[47] to infer activity of TAMs. Based on input RNA-seq count data, this method determines the Macrophage Polarization Index (MPI) and the Activation-induced Macrophage Differentiation Index (AMDI), both with scores that range from −50 to 50. Instead of a category representation, we mapped macrophage activity onto a biological spectrum using this score-based method. More proinflammatory traits are indicated by a higher MPI value, while greater maturity is indicated by a higher AMDI value. Zero was a threshold to designate "pre-activation" or "M0" cells (AMDI < 0, MPI < 0), "M1-transitional" (AMDI < 0, MPI > 0) or "M1-like" cells (AMDI > 0, MPI > 0), and "M2-like" cells (AMDI > 0, MPI < 0), as done by Li et al.[47]

Compared with the T_Mass, microglia of the T_SVZ were more M2-like (from 6.4% to 21.4%) and less M1-like (from 75.1% to 52.8%) and showed an increase in the pre-activation state (from 11.7% to 17.0%, Figure 3C left and middle). Similarly, MDMs of the T_SVZ were predominantly M2-like compared with those in the T_Mass (from 15.4% to 72.6%) and less M1-like (from 59.7% to 27.4%, Figure 3C left and middle). Notably, no MDMs exhibited a pre-activation state in the T_SVZ (from 19.0% in the T_Mass to 0.0% in the T_SVZ, Figure 3C left and middle). In the N_SVZ, as expected, microglia were predominantly M1-like (69.7%) and in the pre-activation state (24.0%) (Figure 3C right). Overall, microglia and MDMs in the T_SVZ were prominently tumor supportive. This suggests that in the T_SVZ, TAMs-specific mechanisms promoting tumor aggressiveness may represent therapeutic vulnerabilities.

To identify potentially targetable genes in the microglia of the T_SVZ, we conducted gene expression analysis and identified the differentially expressed genes (DEGs) in that area compared with the T_Mass and the N_SVZ. The N_SVZ and the T_SVZ had the highest number of unshared DEGs (662) among the comparisons, while the T_Mass and the T_SVZ had the lowest number of unshared DEGs (70, Figure 3D). Moreover, the highest number of shared DEGs was found between N_SVZ-T_Mass and N_SVZ-T_SVZ (1177 DEGs), while the number of shared DEGs between T_Mass-T_SVZ and N_SVZ-T_SVZ, and those between T_Mass-T_SVZ and N_SVZ-T_Mass, were only 112 and 106, respectively. The number of shared DEGs among all three comparisons was 173 (Figure 3D). These data suggest that the T_Mass and the T_SVZ express similar genes, while the N_SVZ is characterized by a different gene set (Figure 3D). Notably, among the DEGs, the CSC master regulator SOX2[41,48] was significantly downregulated in the N_SVZ vs. T_Mass and ZEB1 was significantly downregulated in the N_SVZ vs. T_SVZ (Figure 3E), thus supporting the regulon enrichment results of tumor cells in the T_SVZ (Figure 2D top). Moreover, TFs involved in promotion of neuronal differentiation[49] showed two distinct patterns: while

SOX4 and SOX11 were overexpressed in the T_Mass vs. N_SVZ and in the T_SVZ vs. N_SVZ, SOX5 was significantly upregulated in the N_SVZ vs. T_Mass comparison (Table S2, comparisons as whole areas). Of note, SOX2, SOX4, and SOX11 were upregulated in the T_Mass vs. T_SVZ, and SOX5 was downregulated in the T_Mass vs. T_SVZ. Of note, COL1A1 (a central gene in the dynamic organization of glioma mesenchymal transformation[50]) was downregulated in the T_Mass vs. T_SVZ, further supporting our observation that the T_SVZ microenvironment is characterized by a mesenchymal signature.

When considering overexpressed genes in the T_SVZ as a whole area (i.e., all identified cell types in this microenvironment), SOX2 was upregulated in the T_Mass vs. T_SVZ (Figure 3E top left). The gene encoding for the IL-1R accessory protein (IL-1RAcP) was significantly upregulated in the T_SVZ vs. N_SVZ (Figure 3E top right). Moreover, in addition to GFAP, CD163, PTPRZ1, and ZEB1, we also observed that FZD3, encoding a seven-transmembrane domain receptor of the non-canonical WNT (ncWNT) pathway, was significantly upregulated in the T_SVZ vs. N_SVZ and in the T_Mass vs. N_SVZ (Figure 3E top right; Figure S6 left).

We then performed the same analysis on the microglia only (Table S2, comparisons in microglia). The inflammatory cytokine IL1B[51–58] was significantly upregulated in the T_SVZ vs. T_Mass, suggesting that microglia in the T_SVZ are more inflammatory than those in the T_Mass (Figure 3E bottom left). Two other inflammatory cytokines were upregulated in the T_SVZ microglia: IL15 was significantly upregulated in the T_SVZ vs. T_Mass and in the T_SVZ vs. N_SVZ (Figure 3E bottom left and right), and IL18 was significantly upregulated in the T_SVZ vs. N_SVZ (Figure 3E bottom right), thus confirming that T_SVZ microglia are prominently tumor-supportive and inflammatory, consistent with the results of MacSpectrum (Figure 3C). We confirmed these results by analyzing gene expression of markers of "homeostatic," "activated," and "inflammatory" microglia (Figure S7A). In addition to CD163, CD44, GFAP, and IL2RA, the pro-migration and pro-invasion ncWNT ligand WNT5A[59–63] was significantly upregulated in the T_SVZ vs. N_SVZ and in the T_Mass vs. N_SVZ microglia only comparisons (Figure 3E bottom right; Figure S6 right). Of note, high expression of WNT5A in glioma has been correlated with increased presence of TAMs.[64] Moreover, the putative receptor of WNT5A is FZD3, which was significantly upregulated in the T_SVZ vs. N_SVZ and in the T_Mass vs. N_SVZ whole area comparisons (Figure 3E top right; Figure S6 left).

These results led us to explore the spatial distribution of microglia and tumor cells in cellular neighborhoods of the T_SVZ and the T_Mass microenvironments. We performed spatial transcriptomics using samples from four patients of our cohort with large enough T_SVZ and T_Mass tissues for analyses (Figure 3F). We also profiled the HNS1 sample (one of our two N_SVZ samples). By InferCNV, cell type annotation, and Cell2Location, we first confirmed that most of the cells in the T_Mass and the T_SVZ were tumor cells (except for the GBM4 samples) and that the HNS1 contained normal cells only (Figure S7B). As expected, we found a higher percentage of microglia and GBMmes cells in the T_SVZ samples compared with corresponding T_Mass

samples (Figure S7C). We then quantified the spatial correlations for each patient and each microenvironment and we analyzed the spatial correlations of each cell type vs. microglia and observed different patterns of correlation in the individual patients (Figure 3G). Of note, correlation analyses of microglia in the HNS1 sample revealed significantly weaker correlations with all cell types (Figure 3G). We also observed different patterns of correlations with tumor and normal cells between the T_Mass and the T_SVZ of each patient (Figure S8). To perform statistical analysis of these data and identify spatial correlations that are significantly different between the T_SVZ and the T_Mass microenvironments, we calculated the difference in Pearson's correlation and determined the significance of the difference. This analysis revealed that microglia in the T_SVZ exhibit stronger spatial correlations with tumor cells compared with microglia of the T_Mass (Figure S8L left). Among the four patients, the strongest spatial correlations in the T_SVZ are with GBMmes and GBMnpc for patient GBM4, GBMnpc for patient GBM9, and GBMopc for patients GBM7 and GBM8 (Figure S8L right). We also observed stronger spatial correlation with MDMs and oligodendrocytes in the T_SVZ of two of the four analyzed patients (Figure S8L left). When we examined the patterns of spatial dependencies among cell types,[65] we observed that microglia in the T_SVZ had a high likelihood of communication (Figure 3H) and were both sender and receiver cells in two of the four T_SVZ samples. By contrast, in the T_Mass samples, microglia were only receiver cells, similar to the HNS1 sample (Figures S8M–S8U).

Altogether, these data indicate that the T_SVZ microenvironment is characterized by tumor-supportive microglia that secrete inflammatory cytokines, such as interleukin (IL)-1β, and the pro-migration and pro-invasion ncWNT ligand Wnt-5a. Microglia in the T_SVZ exhibit stronger spatial correlations with tumor cells and establish more spatial dependencies compared with microglia of the T_Mass.

Microglia, not MDMs, establish cell-to-cell interactions with tumor cells in the tumor SVZ microenvironment and are predicted to express IL-1β and Wnt-5a

The spatial coexistence of tumor-supportive, inflammatory microglia and tumor cells and the complex cell-to-cell communication network between microglia, tumor cells, and other cell types in the T_SVZ microenvironment prompted us to further examine their interactions. First, we annotated each identified cluster of our snRNA-seq dataset of T_Mass, T_SVZ, and N_SVZ to identify interactions at high resolution (Figure 4A top). Next, we examined the total number of inferred interactions. The N_SVZ had the lowest number of interactions (221), the T_SVZ had an intermediate number (326), and the T_Mass had the highest number (653) (Figure S9A). These findings correlated with the number of identified clusters (Figure 4A) and suggest that more heterotypic cellular microenvironments, such as those of the T_Mass and the T_SVZ (Figure 1F bottom), contribute to increased cell-to-cell interactions. We then analyzed the number of the incoming and outgoing interactions among cell types. While MDMs exhibited a cell-to-cell communication network in the T_Mass (Figure 4A bottom left), they establish only a few, weak interactions in the T_SVZ (Figure 4A

bottom middle). In contrast, microglia established cell-to-cell communication networks in both the T_Mass (Figure 4A bottom left) and the T_SVZ (Figure 4A bottom middle). In the T_SVZ, microglia showed interactions with different cell types, including tumor cells of the GBMmes state (Figure 4A bottom middle). These data on microglia in the T_SVZ seem to reflect the ability of microglia in the N_SVZ to be highly interactive within the microenvironment and establish a complex cell-to-cell communication network with many cell types (Figure 4A bottom right).

We next studied predicted interactions involving microglia of the T_SVZ. First, we examined predicted interactions within this cell type (microglia to microglia). Activity of the IL-1β –IL-1RAcP pathway was strongly upregulated in "sender" (Figure 4B left) and "receiver" (Figure 4B right) microglia in the T_SVZ compared with microglia of the T_Mass. Specifically, in both analyses the IL-1β –IL-1RAcP pathway was "down" in the T_Mass compared with the T_SVZ (Figure 4B). Second, we examined all predicted incoming (Figure S9B) and outgoing signaling patterns in the T_Mass (Figure 4C left), the T_SVZ (Figure 4C middle), and the N_SVZ (Figure 4C right). Among the incoming signaling pathways of microglia in the T_SVZ, Sema3 and Annexin had the highest relative strength and were specific to this area compared with the T_Mass and the N_SVZ (Figure S9B). Consistent with the DEG analysis (Figure 3E bottom), among the outgoing signaling pathways of microglia in the T_SVZ, ncWNT exhibited the highest relative strength and was specific to this area compared with the T_Mass and the N_SVZ (Figure 4C middle). Of note, ncWNT was also an incoming signaling pathway specific of T_SVZ and exhibited the highest relative strength in clusters of the GBMnpc and GBMopc states (Figure S9B), suggesting a ncWNT-mediated interaction between microglia and tumor cells in the T_SVZ.

We then performed ligand-receptor prediction analyses between microglia as sender cells and any other cell type of the T_SVZ as receiver cells. *WNT5A* is a predicted ligand of microglia, and its predicted receptors are *MCAM* and *FZD3* expressed by endothelial cells and tumor cells of the GBMopc and GBMnpc states, respectively (Figure 4D top). These *WNT5A*-related predictions were specific to the T_SVZ and absent in the T_Mass (Figure 4D bottom; Figures S9C–S9E), in agreement with the incoming and outgoing signaling analyses in the T_SVZ (Figure 4C middle; Figure S9B). The *SPP1-CD44* ligand-receptor combination had the highest communication probability between microglia and tumor cells of the GBMmes state in the T_SVZ (Figure 4D top), between microglia, MDMs, and tumor cells of the GBMac and the GBMmes states in the T_Mass (Figure 4D bottom; Figures S9C and S9D), and between microglia and astrocytes in the N-SVZ (Figure S9E). This is consistent with published work showing that (1) *SPP1-CD44* signaling is present in the glioma perivascular niche,[66] (2) *SPP1* is upregulated[67] and secreted by TAMs in glioma,[68] and (3) *SPP1-CD44* signaling is between TAMs and glioma cells,[69] specifically with GBMmes tumor cells.[70]

Overall, our results revealed that microglia in the T_ SVZ establish cell-to-cell interactions within their cell population and with tumor cells and identify microglia-specific pathways of communications.
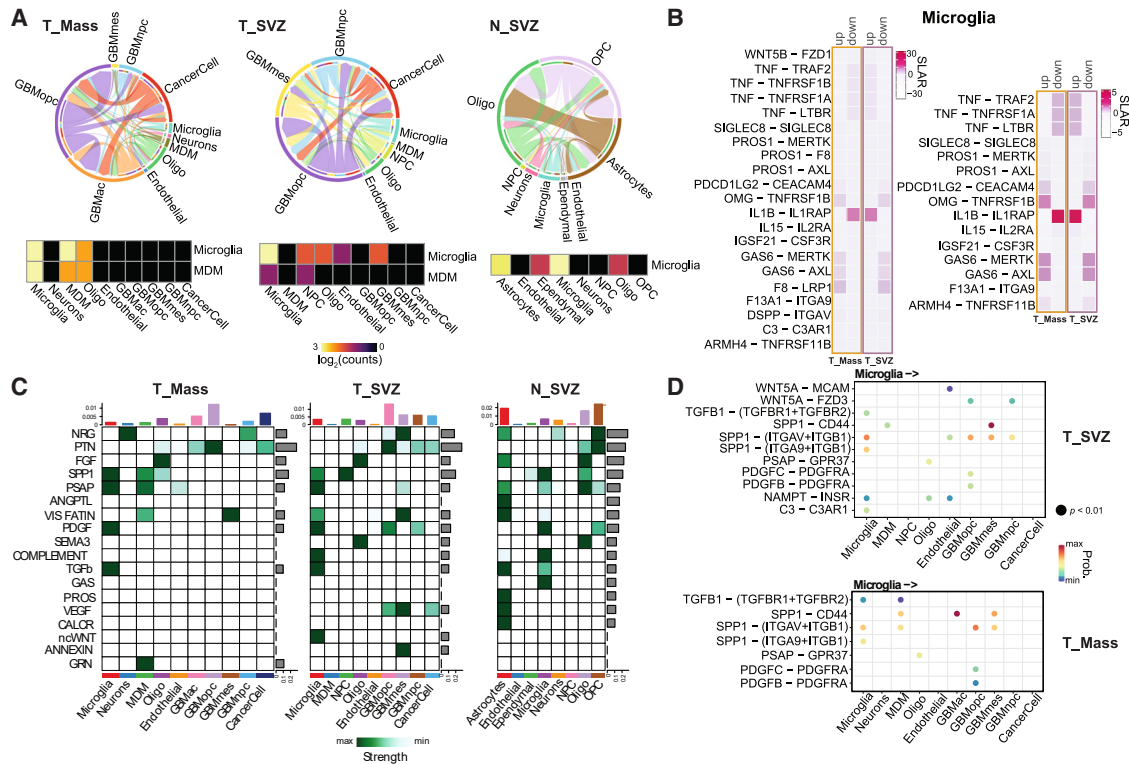
Figure 4. Microglia, not MDMs, establish cell-to-cell interactions with tumor cells in the tumor SVZ microenvironment and are predicted to express IL-1β and Wnt-5a

(A) Incoming and outgoing interactions in the cell-to-cell communication network. Number of interactions between any two cell types shown as circle plots for the T_Mass (top left), T_SVZ (top middle), and N_SVZ (top right). Heatmaps showing the cell-to-cell interactions of microglia and MDM with the other cell types and with themselves for the T_Mass (bottom left), T_SVZ (bottom middle), and N_SVZ (bottom right). No MDMs were present in the N_SVZ, hence only the heatmap for microglia is shown. Color code indicates the log₂ (counts) between 0 and 3.

(B) Heatmaps showing the predicted interactions between sender (left) and receiver (right) cells in the microglia cluster of the T_SVZ. Color code indicates the scaled ligand activity in receiver (SLAR) cells.

(C) Heatmaps of outgoing signaling pathways in the T_Mass (left), T_SVZ (middle), and N_SVZ (right). Color code indicates minimum to maximum strength of each signaling pathway.

(D) Dot plots of ligand-receptor prediction analysis between microglia as ligand-expressing ('sender') cells and any other cell types ('receiver', x axis) in the T_SVZ (top) and in the T_Mass (bottom). Dots indicate $p < 0.01$, color code = minimum to maximum probability. NPC, neural progenitor cells; OPC, oligodendrocyte precursor cells; MDM, monocyte-derived macrophages.

Functional validation of IL-1β/IL1RAcP and Wnt-5a/Frizzled-3 expression in the tumor SVZ

Based on our results revealing that *IL1B* and *WNT5A* are significantly upregulated in the T_SVZ microglia vs. T_Mass and N_SVZ, respectively (Figure 3E bottom left and right), and that their predicted receptors *IL1RAP* (Figure 4B) and *FZD3* (Figure 4D top) are also significantly upregulated in the T_SVZ vs. N_SVZ comparison as whole areas (Figure 3E top right), we next performed functional studies of the IL-1β/IL-1RAcP and Wnt-5a/Frizzled-3 pathways.

First, we defined the cell type expression of *WNT5A*, *IL1B* (Figure 5A top), and of *FZD3*, *IL1RAP* (Figure 5A bottom) in the T_SVZ. While *WNT5A* and *IL1B* were almost exclusively expressed by microglia (Figure 5B), *FZD3* was predominantly expressed by tumor cells of the GBMnpc and GBMopc states, and *IL1RAP* was predominantly expressed by tumor cells of those two states and microglia (Figure 5B). The cell type expression of *WNT5A, IL1B*, *FZD3*, and *IL1RAP* in the T_SVZ overlap-

ped only partially with the expression of the same genes in the T_Mass and the N_SVZ (Figure S10A).

Second, similar to previous work on the role of TAMs in human gliomas, we isolated TAMs using the cd11b enrichment strategy based on immunomagnetic microbeads decorated with recombinantly engineered antibody fragments (Figure 5C) and quantified the levels of Wnt-5a (Figure 5D top) and IL-1β (Figure 5D bottom) secreted by TAMs of matched T_Mass and T_SVZ of four patients. Using immunofluorescence staining, we confirmed that Frizzled-3 (Figure 5E) and IL-1RAcP (Figure 5F left) are expressed by CSCs. For IL-1RAcP, we also confirmed expression at the level of TAMs (Figure 5F right). By staining quantification based on fluorescence intensity, we observed a significantly higher expression of Frizzled-3 in the CSCs isolated from the T_SVZ compared with matched CSCs of the T_Mass (Figure 5E). IL-1RAcP stainings of CSC and TAMs isolated from the T_SVZ and compared with matched T_Mass-derived cells showed a trend toward higher expression in the T_SVZ, and in the case
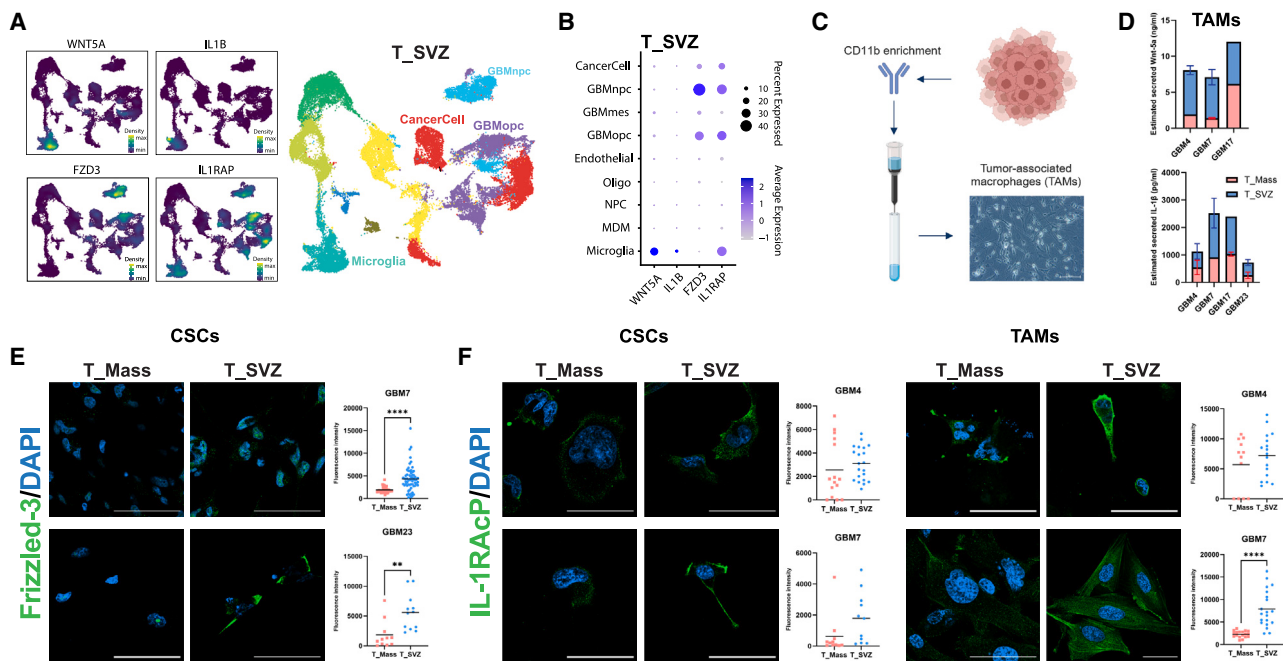
Figure 5. Functional validation of IL-1β/IL1RAcP and Wnt-5a/Frizzled-3 expression in the tumor SVZ

(A) Kernel density estimation UMAPs of the T_SVZ showing expressions of *WNT5A*, *IL1B* (top left) and *FZD3*, *IL1RAP* (bottom left). Cell type annotation of these UMAPs showing the relevant cell types (right).

(B) Dot plot showing cell type expression of *WNT5A*, *IL1B*, *FZD3*, and *IL1RAP* in the T_SVZ.

(C) Schematic of the cd11b enrichment strategy for isolation of tumor-associated macrophages (TAMs). Created with BioRender.com.

(D) Bar graph of estimated Wnt-5a (top) and IL-1β (bottom) secreted from the TAMs isolated from the T_Mass and the T_SVZ of GBM4, 7, 17, and 23 (the latter only for IL-1β; mean ± SEM).

(E) Representative images (left) and staining quantification by fluorescence intensity mean value (right) of cancer stem-like cells (CSCs) isolated from GBM7 (top) and GBM23 (bottom), stained for Frizzled-3 and counterstained with DAPI. Scale bars, 50 μm. **$p < 0.01$, ****$p < 0.0001$ T_Mass-vs. T_SVZ-derived cells.

(F) Representative images and staining quantification by fluorescence intensity mean value of CSCs (left) and TAMs (right) isolated from GBM4 (top) and GBM7 (bottom), stained for IL1-RAcP and counterstained with DAPI. Scale bars, 50 μm. ****$p < 0.0001$ T_Mass-vs. T_SVZ-derived cells.

of TAMs derived from GBM7, the increased expression of IL-1RAcP in the T_SVZ was statistically significant (Figure 5F right). Control stainings (Figure S10B) and control lines, namely the GBM cell line T98G and two commercial cell lines of MDMs and microglia, were stained for Frizzled-3 (T98G, Figure S10C) and IL1-RAcP (T98G, MDM and microglia, Figures S10D and S10E). Of note, the expression of IL-1RAcP in T98G, MDMs, and microglia (Figures S10D and S10E) was lower compared with CSCs and TAMs derived from the T_SVZ (Figure 5F).

IL-1β/IL-1RAcP and Wnt-5a/Frizzled-3 are potential therapeutic targets in the tumor SVZ microenvironment

Given the recognized inflammatory and tumor-supportive role of IL-1β,[51–58] and the pro-migration and pro-invasion functions of Wnt-5a,[59–63] we surmised that strategies to target these two pathways could reveal therapeutic vulnerabilities in the T_SVZ microenvironment. Therefore, we tested the effects of IL-1β/IL-1RAcP and Wnt-5a/Frizzled-3 inhibition *in vitro*.

To evaluate the impact of IL-1β/IL-1RAcP inhibition in TAMs, isolated cd11b-enriched cells from matched T_SVZ and the T_Mass of two patients were treated for 48 h with the anti-IL-1RAcP fully humanized monoclonal antibody nidanilimab (recently renamed as Nadunolimab-CAN04, and currently being

tested in multiple clinical trials[71–73]). We observed significantly reduced IL-1β secretion in nidanilimab-treated TAMs of the T_SVZ in GBM4 (Figure 6A top) and in both the T_Mass and the T_SVZ of GBM7 (Figure 6A bottom). Next, we evaluated the impact of IL-1β/IL-1RAcP inhibition on CSCs. Proliferation of CSCs isolated from the T_Mass and the T_SVZ was significantly reduced after treatment with IL-1β and nidanilimab (Figure 6A right) but not with nidanilimab alone (data not shown), with a more pronounced effect in the T_SVZ compared with T_Mass (Figure 6A right). These data suggest that mimicking the secretion of IL-1β by TAMs is critical for IL-1β/IL-1RAcP inhibition. To test the impact of Wnt-5a/Frizzled-3 inhibition, we performed *in vitro* transwell experiments using CSCs isolated from the T_Mass and the T_SVZ of three patients. Initially, TAMs isolated from matched T_SVZ and the T_Mass of the three patients were treated for 48 h with Box5, a Wnt-5a antagonist. Notably, secretion of Wnt-5a was significantly reduced upon Box5 treatment of TAMs isolated from the T_SVZ (Figure 6B left), suggesting that Box5 may inhibit the Wnt-5a-induced calcium signaling and/or cytokine secretion, as previously described in models of melanoma.[74–76] Exposure of CSCs to conditioned medium of treated or untreated TAMs with Box5 significantly reduced CSC invasion through the transwell (Figure 6B right). In all the
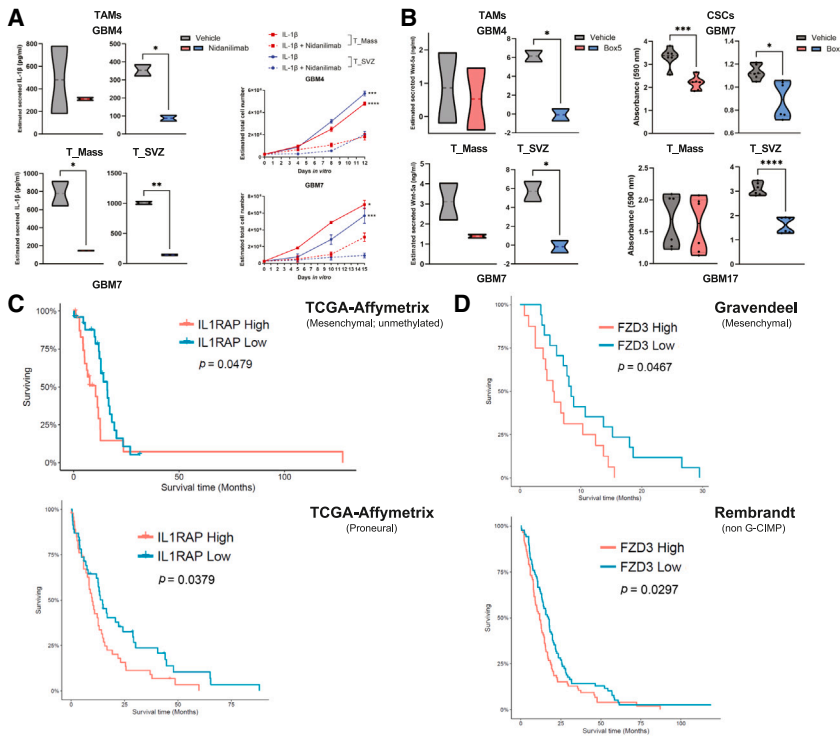
Figure 6. IL-1β/IL1RAcP and Wnt-5a/Frizzled-3 are potential therapeutic targets in the tumor SVZ microenvironment

(A) Truncated violin plots of estimated secreted IL-1β by tumor-associated macrophages (TAMs) isolated from T_Mass and T_SVZ of GBM4 (top) and GBM7 (bottom) after nidanilimab treatment. *$p < 0.05$, **$p < 0.01$ (left). Growth curve analysis (mean ± SEM) of cancer stem-like cells (CSCs) isolated from T_Mass and T_SVZ of GBM4 (top) and GBM7 (bottom) and treated with IL-1β and IL-1β+nidanilimab (right). Nonlinear regression analysis was performed to assess the proliferative potential. *$p < 0.05$, **$p < 0.01$, ***$p < 0.001$, ****$p < 0.0001$ IL-1β vs. IL-1β+nidanilimab.

(B) Truncated violin plots of the estimated secreted Wnt-5a by TAMs isolated from T_Mass and T_SVZ of GBM4 and 7 after treatment with Box5. *$p < 0.05$ (left). Quantification of cell migration based on absorbance of eluted crystal violet used in transwell assays of CSCs isolated from T_Mass and T_SVZ and exposed to conditioned medium of matched TAMs treated with Box5 (right). The results shown here are from GBM7 (top right) and GBM17 (bottom right). *$p < 0.05$, ***$p < 0.001$, ****$p < 0.0001$.

(C) Correlation between *IL1RAP* expression levels and patient survival in the TCGA (Affymetrix platform: mesenchymal; unmethylated, $p = 0.0479$, top and proneural, $p = 0.0379$, bottom).

(D) Correlation between *FZD3* expression levels and patient survival in the Gravendeel's[77] (mesenchymal, $p = 0.0467$, top) and Rembrandt's[78] datasets (non G-CIMP, $p = 0.0297$, bottom). The survival analyses in (C) and (D) were performed using the GlioVis data portal.[79]

analyzed samples, the cells from the T_SVZ consistently showed a significant response to Box5 treatment. However, we also observed a significant reduction in invasion in the CSCs from the T_Mass of GBM7 (Figure 6B right).

To evaluate the clinical significance of our findings, we used public GBM datasets[77,78,80–83] and performed analysis of overall survival based on the expression levels of *IL1RAP* and *FZD3*. High expression of *IL1RAP* and *FZD3* was associated with shorter survival in the TCGA samples (Affymetrix platform, mesenchymal; unmethylated and proneural subtypes, Figure 6C), and in the Gravendeel's[77] (mesenchymal subtype) and Rembrandt's[78] (non G-CIMP) datasets, respectively (Figure 6D).

Altogether, these results indicate that the IL-1β/IL-1RAcP and Wnt-5a/Frizzled-3 represent therapeutic targets in the T_SVZ and have prognostic relevance in subsets of patients with GBM.

DISCUSSION

We built a single-nucleus RNA-sequencing-based microenvironment landscape of the T_SVZ using samples from 15 patients with GBM. We comprehensively compared T_Mass samples isolated from the same patients and used two histologically normal SVZ samples as controls. We identified a *ZEB1*[40–42]-centered mesenchymal signature in the T_SVZ and a tumor-supportive microglia population, which represent the vast majority of TAMs in the T_SVZ microenvironment. These cells spatially coexist and establish cell-to-cell interactions with tumor cells. We systematically characterized these interactions both *in silico*

and *in vitro* and identified two pathways, IL-1β/IL-1RAcP and Wnt-5a/Frizzled-3, representing potential targets in the T_SVZ microenvironment.

Collectively, our findings indicate that the SVZ represents a distinct microenvironment in patients, which is deprived of the GBMac state, is characterized by a mesenchymal signature, and is enriched in tumor-supportive and inflammatory microglia. Moreover, our study identifies potential therapeutic targets in the T_SVZ of patients with GBM.

While it is well recognized that (1) IL-1β is among the most well-characterized inflammatory cytokines in GBM, (2) TAMs secreting IL-1β support tumor growth,[51–58] and (3) microglia (among other cell types) are enriched in an IL-1β inflammatory program,[84] it was still unknown whether TAMs secrete Wnt-5a and if a Wnt-5a-mediated crosstalk exists between TAMs and tumor cells. However, in addition to the known pro-migration and pro-invasion functions of Wnt-5a,[59–63] it has been reported that the expression of Wnt-5a in human glioma is positively correlated with the presence of TAMs.[64]

Our results show that *in vitro* targeting of the IL-1β/IL-1RAcP and Wnt-5a/Frizzled-3 pathways significantly reduces the ability of CSCs of the T_SVZ to proliferate and migrate. Moreover, our analysis of overall survival using public GBM datasets reveals that *IL1RAP* and *FZD3* have prognostic relevance in subsets of patients. Of note, inhibition of the IL-1β/IL-1RAcP pathway with the anti-IL-1RAcP fully humanized monoclonal antibody Nadunolimab-CAN04 is being evaluated in multiple clinical trials of colorectal cancer, non-small cell lung cancer, pancreatic cancer, triple-negative breast cancer,[71–73] and biliary tract cancer

(https://cantargia.com/en/press-releases/cantargia-reports-treatment-of-first-triple-negative-breast-cancer-patient-in-trifour-study).

Given the limited efficacy of current treatments for patients with GBM, our results provide evidence of potential therapeutic opportunities to target the T_SVZ microenvironment. Specifically, inhibiting the IL-1β/IL-1RAcP or the ncWNT (Wnt-5a/Frizzled-3) pathways in the T_SVZ can lead to the reduction of the highly proliferative ability and widespread infiltration of GBM cells in the brain parenchyma.[85] Such an approach could also be combined with strategies aimed at controlling key functional properties of CSCs (self-renewal, chemo-/radio-resistance, metabolic plasticity, survival, etc.) by targeting core intrinsic and extrinsic regulatory networks supporting their stemness and/or by inducing differentiation.

Although microglia undergo changes in gene expression from "homeostatic" to "activated" in diseases of the central nervous system, their diversity and functional roles in human GBM are not fully understood.[86,87] Specifically, their role in spatially distinct GBM microenvironments is still unknown. Recent work identified associations between microglia and the GBMac state.[88] Moreover, microglia were found to be enriched in GBM showing no ventricular contact.[89] However, these studies were not performed on samples taken directly from the SVZ of patients.

By distinguishing between MDMs and microglia, elegant works on the brain tumor microenvironment started to uncover the phenotype of microglia in IDH wild-type/mutant gliomas, and in brain metastases[20,21] and suggested that microglia exhibit an "activated" phenotype in GBM. In addition, two independent groups have shown that in GBM, subsets of microglia upregulate inflammatory (including *IL1B*) and proliferative genes[56] and are characterized by *VEGF-* and *CD163*-expressing cells,[90] suggesting a tumor-supportive function whose mechanisms are still unknown. Future work focused on elucidating the functional role of microglia and their cellular interactions in key areas for the emergence of the recurrent tumor, such as the SVZ, will have important implications for developing effective therapeutic strategies.

Limitations of the study

Our work has some limitations: we have not analyzed the cellular cross-talks mediated by IL-1β and Wnt-5a in other lineages. Specifically, our work is limited to the interactions between microglia and tumor cells in the T_SVZ. Moreover, we have not evaluated the therapeutic efficacy of inhibiting the IL-1β/IL-1RAcP or the ncWNT (Wnt-5a/Frizzled-3) pathways *in vivo*. While inhibition of secreted factors can be challenging due to the dynamics of secretion and the cross-talks between different cell types, disruption of cellular interactions at the level of receptors through blocking antibodies could be a successful approach to develop effective therapies for patients with GBM. Of note, our patient cohort was not powered for the analysis of sex-related differences. Future work will evaluate the therapeutic efficacy of inhibiting the IL-1β/IL-1RAcP and the ncWNT (Wnt-5a/Frizzled-3) pathways in a sex-specific manner.

RESOURCE AVAILABILITY

Lead contact

Further information and requests for resources should be directed to and will be fulfilled by the lead contact, Dr. Sara G.M. Piccirillo (SPiccirillo@salud.unm.edu).

Materials availability

Requests for materials generated in this study should be directed to the lead contact. A completed materials transfer agreement will be required.

Data and code availability

- Raw and processed data to support the findings of this study have been deposited at GEO under accession number GEO: GSE259378 and are publicly available as of the date of publication. This paper also analyzes existing, publicly available datasets; these are listed with accession numbers in the key resources table.
- The data of this manuscript are presented in an interactive shiny app. The app allows users to explore the data, including gene expression, dimensionality reductions and clustering, cell type annotations, markers, and more. Users can also generate their own plots from the data. Data from T_Mass, T_SVZ, and N_SVZ samples are presented here: https://bioinformatics-musc.shinyapps.io/sara_piccirillo_glioblastoma/
- The custom code used is available from GitHub at: https://github.com/BioinformaticsMUSC/PiccirilloLabEtAl_Glioblastoma. The code has also been deposited at Zenodo: https://doi.org/10.5281/zenodo.14183518 and is publicly available as of the date of publication.
- All other data supporting the findings of this study are available from the lead contact upon reasonable request.

AUTHOR CONTRIBUTIONS

S.G.M.P. designed and supervised the study. S.G.M.P, Y.L.-M., S.S., B.G., and S.B. wrote the manuscript. S.G.M.P. coordinated experiments. Y.L.-M., V.A., and F.M. carried out the experiments and contributed to data interpretation. L.A.G.-M. performed analysis of the datasets available through the GlioVis portal. S.V. assisted with the collection and curation of clinical data. S.S., B.G., D.M., and S.B. wrote all original code used in the study and

performed bioinformatic analysis. E.P., M.K., M.O.C., and C.A.B. provided patient tissue samples. All authors reviewed and approved the manuscript.

STAR★METHODS

Detailed methods are provided in the online version of this paper and include the following:

- KEY RESOURCES TABLE
- EXPERIMENTAL MODEL AND STUDY PARTICIPANT DETAILS
  - Glioblastoma patient samples
  - Establishment and propagation of patient-derived cancer stem-like cells
  - Establishment of patient-derived tumor-associated macrophages
- METHOD DETAILS
  - 5-ALA administration and patient sample collection
  - Genomic DNA sequencing
  - Mutation, copy-number and gene expression data
  - Single-nucleus RNA-sequencing
  - Definition of malignant cells
  - Cellular dynamics
  - Gene regulatory networks
  - Identification of differentially expressed genes
  - Expression analysis of the SCENIC-identified ZEB1 targets
  - Cell-cell interaction analysis
  - Pathway and MacSpectrum analyses
  - Spatial transcriptomics
  - 10x Genomics Visium analysis
  - Definition of malignant spot
  - 10x Visium spot deconvolution
  - 10x Genomics Visium sample clustering
  - 10x Genomics Visium spot clustering and intracellular communication
  - 10x Visium microglia spatial correlation
  - CD11b enrichment
  - IL-1β and Wnt-5a ELISA
  - IL-1RAcP and Frizzled-3 immunofluorescence
  - *In vitro* treatment assay
  - Survival analysis
- QUANTIFICATION AND STATISTICAL ANALYSIS

REFERENCES

1. Stupp, R., Mason, W.P., van den Bent, M.J., Weller, M., Fisher, B., Taphoorn, M.J.B., Belanger, K., Brandes, A.A., and Marosi, C. (2005). Radiotherapy plus concomitant and adjuvant temozolomide for glioblastoma. N. Engl. J. Med. *352*, 987–996. https://doi.org/10.1056/NEJMoa043330.

2. Wen, P.Y., and Kesari, S. (2008). Malignant gliomas in adults. N. Engl. J. Med. *359*, 492–507. https://doi.org/10.1056/NEJMra0708126.

3. Ostrom, Q.T., Price, M., Neff, C., Cioffi, G., Waite, K.A., Kruchko, C., and Barnholtz-Sloan, J.S. (2023). CBTRUS Statistical Report: Primary Brain and Other Central Nervous System Tumors Diagnosed in the United States in 2016-2020. Neuro Oncol. *25*, iv1–iv99. https://doi.org/10.1093/neuonc/noad149.

4. Piccirillo, S.G., Spiteri, I., Sottoriva, A., Touloumis, A., Ber, S., Price, S.J., Heywood, R., Francis, N.J., Howarth, K.D., Collins, V.P., et al. (2015). Contributions to drug resistance in glioblastoma derived from malignant cells in the sub-ependymal zone. Cancer Res. *75*, 194–202. https://doi.org/10.1158/0008-5472.CAN-13-3131.

5. Spiteri, I., Caravagna, G., Cresswell, G.D., Vatsiou, A., Nichol, D., Acar, A., Ermini, L., Chkhaidze, K., Werner, B., Mair, R., et al. (2019). Evolutionary dynamics of residual disease in human glioblastoma. Ann. Oncol. *30*, 456–463. https://doi.org/10.1093/annonc/mdy506.

6. Markovic, D.S., Vinnakota, K., Chirasani, S., Synowitz, M., Raguet, H., Stock, K., Sliwa, M., Lehmann, S., Kälin, R., van Rooijen, N., et al. (2009). Gliomas induce and exploit microglial MT1-MMP expression for tumor expansion. Proc. Natl. Acad. Sci. USA *106*, 12530–12535. https://doi.org/10.1073/pnas.0804273106.

7. Coniglio, S.J., Eugenin, E., Dobrenis, K., Stanley, E.R., West, B.L., Symons, M.H., and Segall, J.E. (2012). Microglial stimulation of glioblastoma invasion involves epidermal growth factor receptor (EGFR) and colony stimulating factor 1 receptor (CSF-1R) signaling. Mol. Med. *18*, 519–527. https://doi.org/10.2119/molmed.2011.00217.

8. Pyonteck, S.M., Akkari, L., Schuhmacher, A.J., Bowman, R.L., Sevenich, L., Quail, D.F., Olson, O.C., Quick, M.L., Huse, J.T., Teijeiro, V., et al. (2013). CSF-1R inhibition alters macrophage polarization and blocks glioma progression. Nat. Med. *19*, 1264–1272. https://doi.org/10.1038/nm.3337.

9. Zhou, W., Ke, S.Q., Huang, Z., Flavahan, W., Fang, X., Paul, J., Wu, L., Sloan, A.E., McLendon, R.E., Li, X., et al. (2015). Periostin secreted by glioblastoma stem cells recruits M2 tumour-associated macrophages and promotes malignant growth. Nat. Cell Biol. *17*, 170–182. https://doi.org/10.1038/ncb3090.

10. Gabrusiewicz, K., Rodriguez, B., Wei, J., Hashimoto, Y., Healy, L.M., Maiti, S.N., Thomas, G., Zhou, S., Wang, Q., Elakkad, A., et al. (2016). Glioblastoma-infiltrated innate immune cells resemble M0 macrophage phenotype. JCI Insight *1*, e85841. https://doi.org/10.1172/jci.insight.85841.

11. Bowman, R.L., Klemm, F., Akkari, L., Pyonteck, S.M., Sevenich, L., Quail, D.F., Dhara, S., Simpson, K., Gardner, E.E., Iacobuzio-Donahue, C.A., et al. (2016). Macrophage Ontogeny Underlies Differences in Tumor-Specific Education in Brain Malignancies. Cell Rep. *17*, 2445–2459. https://doi.org/10.1016/j.celrep.2016.10.052.

12. Shi, Y., Ping, Y.F., Zhou, W., He, Z.C., Chen, C., Bian, B.S.J., Zhang, L., Chen, L., Lan, X., Zhang, X.C., et al. (2017). Tumour-associated macrophages secrete pleiotrophin to promote PTPRZ1 signalling in glioblastoma stem cells for tumour growth. Nat. Commun. *8*, 15080. https://doi.org/10.1038/ncomms15080.

13. Wang, Q., Hu, B., Hu, X., Kim, H., Squatrito, M., Scarpace, L., deCarvalho, A.C., Lyu, S., Li, P., Li, Y., et al. (2017). Tumor Evolution of Glioma-Intrinsic Gene Expression Subtypes Associates with Immunological Changes in the Microenvironment. Cancer Cell *32*, 42–56.e6. https://doi.org/10.1016/j.ccell.2017.06.003.

14. Darmanis, S., Sloan, S.A., Croote, D., Mignardi, M., Chernikova, S., Samghababi, P., Zhang, Y., Neff, N., Kowarsky, M., Caneda, C., et al. (2017). Single-Cell RNA-Seq Analysis of Infiltrating Neoplastic Cells at the Migrating Front of Human Glioblastoma. Cell Rep. *21*, 1399–1410. https://doi.org/10.1016/j.celrep.2017.10.030.

15. Müller, S., Kohanbash, G., Liu, S.J., Alvarado, B., Carrera, D., Bhaduri, A., Watchmaker, P.B., Yagnik, G., and Lullo, E. (2017). Single-cell profiling of human gliomas reveals macrophage ontogeny as a basis for regional differences in macrophage activation in the tumor microenvironment. Genome Biol. *18*, 234. https://doi.org/10.1186/s13059-017-1362-4.

16. Neftel, C., Laffy, J., Filbin, M.G., Hara, T., Shore, M.E., Rahme, G.J., Richman, A.R., Silverbush, D., Shaw, M.L., Hebert, C.M., et al. (2019). An

Integrative Model of Cellular States, Plasticity, and Genetics for Glioblastoma. Cell 178, 835–849.e21. https://doi.org/10.1016/j.cell.2019.06.024.

17. Takenaka, M.C., Gabriely, G., Rothhammer, V., Mascanfroni, I.D., Wheeler, M.A., Chao, C.C., Gutiérrez-Vázquez, C., Kenison, J., Tjon, E.C., Barroso, A., et al. (2019). Control of tumor-associated macrophages and T cells in glioblastoma via AHR and CD39. Nat. Neurosci. 22, 729–740. https://doi.org/10.1038/s41593-019-0370-y.

18. Kaffes, I., Szulzewsky, F., Chen, Z., Herting, C.J., Gabanic, B., Velázquez Vega, J.E., Shelton, J., Switchenko, J.M., Ross, J.L., McSwain, L.F., et al. (2019). Human Mesenchymal glioblastomas are characterized by an increased immune cell presence compared to Proneural and Classical tumors. OncoImmunology 8, e1655360. https://doi.org/10.1080/2162402X.2019.1655360.

19. Chen, P., Hsu, W.H., Chang, A., Tan, Z., Lan, Z., Zhou, A., Spring, D.J., Lang, F.F., Wang, Y.A., and DePinho, R.A. (2020). Circadian Regulator CLOCK Recruits Immune-Suppressive Microglia into the GBM Tumor Microenvironment. Cancer Discov. 10, 371–381. https://doi.org/10.1158/2159-8290.CD-19-0400.

20. Friebel, E., Kapolou, K., Unger, S., Núñez, N.G., Utz, S., Rushing, E.J., Regli, L., Weller, M., Greter, M., Tugues, S., et al. (2020). Single-Cell Mapping of Human Brain Cancer Reveals Tumor-Specific Instruction of Tissue-Invading Leukocytes. Cell 181, 1626–1642.e20. https://doi.org/10.1016/j.cell.2020.04.055.

21. Klemm, F., Maas, R.R., Bowman, R.L., Kornete, M., Soukup, K., Nassiri, S., Brouland, J.P., Iacobuzio-Donahue, C.A., Brennan, C., Tabar, V., et al. (2020). Interrogation of the Microenvironmental Landscape in Brain Tumors Reveals Disease-Specific Alterations of Immune Cells. Cell 181, 1643–1660.e17. https://doi.org/10.1016/j.cell.2020.05.007.

22. Landry, A.P., Balas, M., Alli, S., Spears, J., and Zador, Z. (2020). Distinct regional ontogeny and activation of tumor associated macrophages in human glioblastoma. Sci. Rep. 10, 19542. https://doi.org/10.1038/s41598-020-76657-3.

23. Ochocka, N., Segit, P., Walentynowicz, K.A., Wojnicki, K., Cyranowski, S., Swatler, J., Mieczkowski, J., and Kaminska, B. (2021). Single-cell RNA sequencing reveals functional heterogeneity of glioma-associated brain macrophages. Nat. Commun. 12, 1151. https://doi.org/10.1038/s41467-021-21407-w.

24. Pombo Antunes, A.R., Scheyltjens, I., Lodi, F., Messiaen, J., Antoranz, A., Duerinck, J., Kancheva, D., Martens, L., De Vlaminck, K., Van Hove, H., et al. (2021). Single-cell profiling of myeloid cells in glioblastoma across species and disease stage reveals macrophage competition and specialization. Nat. Neurosci. 24, 595–610. https://doi.org/10.1038/s41593-020-00789-y.

25. Ravi, V.M., Neidert, N., Will, P., Joseph, K., Maier, J.P., Kückelhaus, J., Vollmer, L., Goeldner, J.M., Behringer, S.P., Scherer, F., et al. (2022). T-cell dysfunction in the glioblastoma microenvironment is mediated by myeloid cells releasing interleukin-10. Nat. Commun. 13, 925. https://doi.org/10.1038/s41467-022-28523-1.

26. Ravi, V.M., Will, P., Kueckelhaus, J., Sun, N., Joseph, K., Salié, H., Vollmer, L., Kuliesiute, U., Follo, M., Scherer, F., et al. (2022). Spatially resolved multi-omics deciphers bidirectional tumor-host interdependence in glioblastoma. Cancer Cell 40, 639–655.e13. https://doi.org/10.1016/j.ccell.2022.05.009.

27. Yin, W., Ping, Y.F., Li, F., Lv, S.Q., Zhang, X.N., Li, X.G., Guo, Y., Liu, Q., Li, T.R., Yang, L.Q., et al. (2022). A map of the spatial distribution and tumour-associated macrophage states in glioblastoma and grade 4 IDH-mutant astrocytoma. J. Pathol. 258, 121–135. https://doi.org/10.1002/path.5984.

28. Kim, H.J., Park, J.H., Kim, H.C., Kim, C.W., Kang, I., and Lee, H.K. (2022). Blood monocyte-derived CD169+ macrophages contribute to antitumor immunity against glioblastoma. Nat. Commun. 13, 6211. https://doi.org/10.1038/s41467-022-34001-5.

29. Garcia-Montano, L.A., Licon-Munoz, Y., Martinez, F.J., Keddari, Y.R., Ziemke, M.K., Chohan, M.O., and Piccirillo, S.G.M. (2023). Dissecting Intra-tumor Heterogeneity in the Glioblastoma Microenvironment Using Fluorescence-Guided Multiple Sampling. Mol. Cancer Res. OF1-OF13, 755–767. https://doi.org/10.1158/1541-7786.MCR-23-0048.

30. Brennan, C.W., Verhaak, R.G.W., McKenna, A., Campos, B., Noushmehr, H., Salama, S.R., Zheng, S., Chakravarty, D., Sanborn, J.Z., Berman, S.H., et al. (2013). The somatic genomic landscape of glioblastoma. Cell 155, 462–477. https://doi.org/10.1016/j.cell.2013.09.034.

31. Ceccarelli, M., Barthel, F.P., Malta, T.M., Sabedot, T.S., Salama, S.R., Murray, B.A., Morozova, O., Newton, Y., Radenbaugh, A., Pagnotta, S.M., et al. (2016). Molecular Profiling Reveals Biologically Discrete Subsets and Pathways of Progression in Diffuse Glioma. Cell 164, 550–563. https://doi.org/10.1016/j.cell.2015.12.028.

32. Durante, M.A., Rodriguez, D.A., Kurtenbach, S., Kuznetsov, J.N., Sanchez, M.I., Decatur, C.L., Snyder, H., Feun, L.G., Livingstone, A.S., and Harbour, J.W. (2020). Single-cell analysis reveals new evolutionary complexity in uveal melanoma. Nat. Commun. 11, 496. https://doi.org/10.1038/s41467-019-14256-1.

33. Couturier, C.P., Nadaf, J., Li, Z., Baig, S., Riva, G., Le, P., Kloosterman, D.J., Monlong, J., Nkili Meyong, A., Allache, R., et al. (2022). Glioblastoma scRNA-seq shows treatment-induced, immune-dependent increase in mesenchymal cancer cells and structural variants in distal neural stem cells. Neuro Oncol. 24, 1494–1508. https://doi.org/10.1093/neuonc/noac085.

34. Lange, M., Bergen, V., Klein, M., Setty, M., Reuter, B., Bakhti, M., Lickert, H., Ansari, M., Schniering, J., Schiller, H.B., et al. (2022). CellRank for directed single-cell fate mapping. Nat. Methods 19, 159–170. https://doi.org/10.1038/s41592-021-01346-6.

35. Weiler, P., Lange, M., Klein, M., Pe'er, D., and Theis, F. (2024). CellRank 2: unified fate mapping in multiview single-cell data. Nat. Methods 21, 1196–1205. https://doi.org/10.1038/s41592-024-02303-9.

36. Aibar, S., González-Blas, C.B., Moerman, T., Huynh-Thu, V.A., Imrichova, H., Hulselmans, G., Rambow, F., Marine, J.C., Geurts, P., Aerts, J., et al. (2017). SCENIC: single-cell regulatory network inference and clustering. Nat. Methods 14, 1083–1086. https://doi.org/10.1038/nmeth.4463.

37. Van de Sande, B., Flerin, C., Davie, K., De Waegeneer, M., Hulselmans, G., Aibar, S., Seurinck, R., Saelens, W., Cannoodt, R., Rouchon, Q., et al. (2020). A scalable SCENIC workflow for single-cell gene regulatory network analysis. Nat. Protoc. 15, 2247–2276. https://doi.org/10.1038/s41596-020-0336-2.

38. Tome-Garcia, J., Erfani, P., Nudelman, G., Tsankov, A.M., Katsyv, I., Tejero, R., Zhang, B., Walsh, M., Friedel, R.H., Zaslavsky, E., and Tsankova, N.M. (2018). Analysis of chromatin accessibility uncovers TEAD1 as a regulator of migration in human glioblastoma. Nat. Commun. 9, 4020. https://doi.org/10.1038/s41467-018-06258-2.

39. Barrette, A.M., Ronk, H., Joshi, T., Mussa, Z., Mehrotra, M., Bouras, A., Nudelman, G., Jesu Raj, J.G., Bozec, D., Lam, W., et al. (2022). Anti-invasive efficacy and survival benefit of the YAP-TEAD inhibitor verteporfin in preclinical glioblastoma models. Neuro Oncol. 24, 694–707. https://doi.org/10.1093/neuonc/noab244.

40. Siebzehnrubl, F.A., Silver, D.J., Tugertimur, B., Deleyrolle, L.P., Siebzehnrubl, D., Sarkisian, M.R., Devers, K.G., Yachnis, A.T., Kupper, M.D., Neal, D., et al. (2013). The ZEB1 pathway links glioblastoma initiation, invasion and chemoresistance. EMBO Mol. Med. 5, 1196–1212. https://doi.org/10.1002/emmm.201302827.

41. Singh, D.K., Kollipara, R.K., Vemireddy, V., Yang, X.L., Sun, Y., Regmi, N., Klingler, S., Hatanpaa, K.J., Raisanen, J., Cho, S.K., et al. (2017). Oncogenes Activate an Autonomous Transcriptional Regulatory Circuit That Drives Glioblastoma. Cell Rep. 18, 961–976. https://doi.org/10.1016/j.celrep.2016.12.064.

42. Chandra, A., Jahangiri, A., Chen, W., Nguyen, A.T., Yagnik, G., Pereira, M.P., Jain, S., Garcia, J.H., Shah, S.S., Wadhwa, H., et al. (2020). Clonal ZEB1-Driven Mesenchymal Transition Promotes Targetable Oncologic

Antiangiogenic Therapy Resistance. Cancer Res. *80*, 1498–1511. https://doi.org/10.1158/0008-5472.CAN-19-1305.

43. Mossi Albiach, A.J.,J., Kapustova, I., Kvedaraite, E., Codeluppi, S., Munting, J.B., Borm, L.E., Jacobsen, J.K., Shamikh, A., Persson, O., and Linnarsson, S. (2023). Glioblastoma is spatially organized by neurodevelopmental programs and a glial-like wound healing response. Preprint at bioRxiv. https://doi.org/10.1101/2023.09.01.555882.

44. Jing, S., Chen, L., Han, S., Liu, N., Han, M., Yang, Y., and Yan, C. (2021). Expression of TCF7L2 in Glioma and Its Relationship With Clinicopathological Characteristics and Patient Overall Survival. Front. Neurol. *12*, 627431. https://doi.org/10.3389/fneur.2021.627431.

45. Nixon, B.G., Kuo, F., Ji, L., Liu, M., Capistrano, K., Do, M., Franklin, R.A., Wu, X., Kansler, E.R., Srivastava, R.M., et al. (2022). Tumor-associated macrophages expressing the transcription factor IRF8 promote T cell exhaustion in cancer. Immunity *55*, 2044–2058.e5. https://doi.org/10.1016/j.immuni.2022.10.002.

46. Masuda, T., Tsuda, M., Yoshinaga, R., Tozaki-Saitoh, H., Ozato, K., Tamura, T., and Inoue, K. (2012). IRF8 is a critical transcription factor for transforming microglia into a reactive phenotype. Cell Rep. *1*, 334–340. https://doi.org/10.1016/j.celrep.2012.02.014.

47. Li, C., Menoret, A., Farragher, C., Ouyang, Z., Bonin, C., Holvoet, P., Vella, A.T., and Zhou, B. (2019). Single cell transcriptomics based-MacSpectrum reveals novel macrophage activation signatures in diseases. JCI Insight *5*, e126453. https://doi.org/10.1172/jci.insight.126453.

48. Suvà, M.L., Rheinbay, E., Gillespie, S.M., Patel, A.P., Wakimoto, H., Rabkin, S.D., Riggi, N., Chi, A.S., Cahill, D.P., Nahed, B.V., et al. (2014). Reconstructing and reprogramming the tumor-propagating potential of glioblastoma stem-like cells. Cell *157*, 580–594. https://doi.org/10.1016/j.cell.2014.02.030.

49. Stevanovic, M., Drakulic, D., Lazic, A., Ninkovic, D.S., Schwirtlich, M., and Mojsin, M. (2021). SOX Transcription Factors as Important Regulators of Neuronal and Glial Differentiation During Nervous System Development and Adult Neurogenesis. Front. Mol. Neurosci. *14*, 654031. https://doi.org/10.3389/fnmol.2021.654031.

50. Comba, A., Faisal, S.M., Dunn, P.J., Argento, A.E., Hollon, T.C., Al-Holou, W.N., Varela, M.L., Zamler, D.B., Quass, G.L., Apostolides, P.F., et al. (2022). Spatiotemporal analysis of glioma heterogeneity reveals COL1A1 as an actionable target to disrupt tumor progression. Nat. Commun. *13*, 3606. https://doi.org/10.1038/s41467-022-31340-1.

51. Sarkar, S., and Yong, V.W. (2009). Inflammatory cytokine modulation of matrix metalloproteinase expression and invasiveness of glioma cells in a 3-dimensional collagen matrix. J. Neuro Oncol. *91*, 157–164. https://doi.org/10.1007/s11060-008-9695-1.

52. Li, Y., Wang, L., Pappan, L., Galliher-Beckley, A., and Shi, J. (2012). IL-1β promotes stemness and invasiveness of colon cancer cells through Zeb1 activation. Mol. Cancer *11*, 87. https://doi.org/10.1186/1476-4598-11-87.

53. Carmi, Y., Dotan, S., Rider, P., Kaplanov, I., White, M.R., Baron, R., Abutbul, S., Huszar, M., Dinarello, C.A., Apte, R.N., and Voronov, E. (2013). The role of IL-1β in the early tumor cell–induced angiogenic response. J. Immunol. *190*, 3500–3509. https://doi.org/10.4049/jimmunol.1202769.

54. Herting, C.J., Chen, Z., Maximov, V., Duffy, A., Szulzewsky, F., Shayakhmetov, D.M., and Hambardzumyan, D. (2019). Tumour-associated macrophage-derived interleukin-1 mediates glioblastoma-associated cerebral oedema. Brain *142*, 3834–3851. https://doi.org/10.1093/brain/awz331.

55. Bayik, D., Zhou, Y., Park, C., Hong, C., Vail, D., Silver, D.J., Lauko, A., Roversi, G., Watson, D.C., Lo, A., et al. (2020). Myeloid-Derived Suppressor Cell Subsets Drive Glioblastoma Growth in a Sex-Specific Manner. Cancer Discov. *10*, 1210–1225. https://doi.org/10.1158/2159-8290.CD-19-1355.

56. Liu, H., Sun, Y., Zhang, Q., Jin, W., Gordon, R.E., Zhang, Y., Wang, J., Sun, C., Wang, Z.J., Qi, X., et al. (2021). Pro-inflammatory and prolifera-

57. Kai, K., Komohara, Y., Esumi, S., Fujiwara, Y., Yamamoto, T., Uekawa, K., Ohta, K., Takezaki, T., Kuroda, J., Shinojima, N., et al. (2022). Microglia and brain macrophages as drivers of glioma progression. Hum. Cell *35*, 226–237. https://doi.org/10.1007/s13577-021-00619-8.

58. Chen, Z., Giotti, B., Kaluzova, M., Vallcorba, M.P., Rawat, K., Price, G., Herting, C.J., Pinero, G., Cristea, S., Ross, J.L., et al. (2023). A paracrine circuit of IL-1beta/IL-1R1 between myeloid and tumor cells drives genotype-dependent glioblastoma progression. J. Clin. Invest. *133*, e163802. https://doi.org/10.1172/JCI163802.

59. Kamino, M., Kishida, M., Kibe, T., Ikoma, K., Iijima, M., Hirano, H., Tokudome, M., Chen, L., Koriyama, C., Yamada, K., et al. (2011). Wnt-5a signaling is correlated with infiltrative activity in human glioma by inducing cellular migration and MMP-2. Cancer Sci. *102*, 540–548. https://doi.org/10.1111/j.1349-7006.2010.01815.x.

60. Hu, B., Wang, Q., Wang, Y.A., Hua, S., Sauvé, C.E.G., Ong, D., Lan, Z.D., Chang, Q., Ho, Y.W., Monasterio, M.M., et al. (2016). Epigenetic Activation of WNT5A Drives Glioblastoma Stem Cell Differentiation and Invasive Growth. Cell *167*, 1281–1295.e18. https://doi.org/10.1016/j.cell.2016.10.039.

61. Binda, E., Visioli, A., Giani, F., Trivieri, N., Palumbo, O., Restelli, S., Dezi, F., Mazza, T., Fusilli, C., Legnani, F., et al. (2017). Wnt5a Drives an Invasive Phenotype in Human Glioblastoma Stem-like Cells. Cancer Res. *77*, 996–1007. https://doi.org/10.1158/0008-5472.CAN-16-1693.

62. Liu, G., Yan, T., Li, X., Sun, J., Zhang, B., Wang, H., and Zhu, Y. (2018). Daam1 activates RhoA to regulate Wnt5a-induced glioblastoma cell invasion. Oncol. Rep. *39*, 465–472. https://doi.org/10.3892/or.2017.6124.

63. Trivieri, N., Visioli, A., Mencarelli, G., Cariglia, M.G., Marongiu, L., Pracella, R., Giani, F., Soriano, A.A., Barile, C., Cajola, L., et al. (2022). Growth factor independence underpins a paroxysmal, aggressive Wnt5aHigh/EphA2Low phenotype in glioblastoma stem cells, conducive to experimental combinatorial therapy. J. Exp. Clin. Cancer Res. *41*, 139. https://doi.org/10.1186/s13046-022-02333-1.

64. Dijksterhuis, J.P., Arthofer, E., Marinescu, V.D., Nelander, S., Uhlén, M., Pontén, F., Mulder, J., and Schulte, G. (2015). High levels of WNT-5A in human glioma correlate with increased presence of tumor-associated microglia/monocytes. Exp. Cell Res. *339*, 280–288. https://doi.org/10.1016/j.yexcr.2015.10.022.

65. Fischer, D.S., Schaar, A.C., and Theis, F.J. (2023). Modeling intercellular communication in tissues using spatial graphs of cells. Nat. Biotechnol. *41*, 332–336. https://doi.org/10.1038/s41587-022-01467-z.

66. Pietras, A., Katz, A.M., Ekström, E.J., Wee, B., Halliday, J.J., Pitter, K.L., Werbeck, J.L., Amankulor, N.M., Huse, J.T., and Holland, E.C. (2014). Osteopontin-CD44 signaling in the glioma perivascular niche enhances cancer stem cell phenotypes and promotes aggressive tumor growth. Cell Stem Cell *14*, 357–369. https://doi.org/10.1016/j.stem.2014.01.005.

67. Szulzewsky, F., Pelz, A., Feng, X., Synowitz, M., Markovic, D., Langmann, T., Holtman, I.R., Wang, X., Eggen, B.J.L., Boddeke, H.W.G.M., et al. (2015). Glioma-associated microglia/macrophages display an expression profile different from M1 and M2 polarization and highly express Gpnmb and Spp1. PLoS One *10*, e0116644. https://doi.org/10.1371/journal.pone.0116644.

68. Chen, P., Zhao, D., Li, J., Liang, X., Li, J., Chang, A., Henry, V.K., Lan, Z., Spring, D.J., Rao, G., et al. (2019). Symbiotic Macrophage-Glioma Cell Interactions Reveal Synthetic Lethality in PTEN-Null Glioma. Cancer Cell *35*, 868–884.e6. https://doi.org/10.1016/j.ccell.2019.05.003.

69. Abdelfattah, N., Kumar, P., Wang, C., Leu, J.S., Flynn, W.F., Gao, R., Baskin, D.S., Pichumani, K., Ijare, O.B., Wood, S.L., et al. (2022). Single-cell analysis of human glioma and immune cells identifies S100A4 as an immunotherapy target. Nat. Commun. *13*, 767. https://doi.org/10.1038/s41467-022-28372-y.

70. He, C., Sheng, L., Pan, D., Jiang, S., Ding, L., Ma, X., Liu, Y., and Jia, D. (2021). Single-Cell Transcriptomic Analysis Revealed a Critical Role of

tive microglia drive progression of glioblastoma. Cell Rep. *36*, 109718. https://doi.org/10.1016/j.celrep.2021.109718.

SPP1/CD44-Mediated Crosstalk Between Macrophages and Cancer Cells in Glioma. Front. Cell Dev. Biol. *9*, 779319. https://doi.org/10.3389/fcell.2021.779319.

71. Robbrecht, D., Jungels, C., Sorensen, M.M., Spanggaard, I., Eskens, F., Fretland, S.Ø., Guren, T.K., Aftimos, P., Liberg, D., Svedman, C., et al. (2022). First-in-human phase 1 dose-escalation study of CAN04, a first-in-class interleukin-1 receptor accessory protein (IL1RAP) antibody in patients with solid tumours. Br. J. Cancer *126*, 1010–1017. https://doi.org/10.1038/s41416-021-01657-7.

72. Paulus, A., Cicenas, S., Zvirbule, Z., Paz-Ares, L., Awada, A., Garcia-Ribas, I., Losic, N., and Zemaitis, M. (2022). Phase 1/2a trial of nadunolimab, a first-in-class fully humanized monoclonal antibody against IL1-RAP, in combination with cisplatin and gemcitabine (CG) in patients with non-small cell lung cancer (NSCLC). J. Clin. Oncol. *40*, 9020. https://doi.org/10.1200/JCO.2022.40.16_suppl.9020.

73. Van Cutsem, E., Løvendahl Eefsen, R., Ochsenreither, S., Zvirbule, Z., Ivanauskas, A., Arnold, D., Baltruskeviciene, E., Pfeiffer, P., Yachnin, J., Garcia-Carbonero, R., Greil, R., et al. (2022). Phase 1/2a trial of nadunolimab, a first-in-class fully humanized monoclonal antibody against IL1RAP, in combination with gemcitabine and nab-paclitaxel (GN) in patients with pancreatic adenocarcinoma (PDAC). J. Clin. Oncol. *40*, 4141. https://doi.org/10.1200/JCO.2022.40.16_suppl.4141.

74. Jenei, V., Sherwood, V., Howlin, J., Linnskog, R., Säfholm, A., Axelsson, L., and Andersson, T. (2009). A t-butyloxycarbonyl-modified Wnt5a-derived hexapeptide functions as a potent antagonist of Wnt5a-dependent melanoma cell invasion. Proc. Natl. Acad. Sci. USA *106*, 19473–19478. https://doi.org/10.1073/pnas.0909409106.

75. Ekström, E.J., Bergenfelz, C., von Bulow, V., Serifler, F., Carlemalm, E., Jonsson, G., Andersson, T., and Leandersson, K. (2014). WNT5A induces release of exosomes containing pro-angiogenic and immunosuppressive factors from malignant melanoma cells. Mol. Cancer *13*, 88. https://doi.org/10.1186/1476-4598-13-88.

76. Linnskog, R., Mohapatra, P., Moradi, F., Prasad, C.P., and Andersson, T. (2016). Demonstration of a WNT5A-IL-6 positive feedback loop in melanoma cells: Dual interference of this loop more effectively impairs melanoma cell invasion. Oncotarget *7*, 37790–37802. https://doi.org/10.18632/oncotarget.9332.

77. Gravendeel, L.A.M., Kouwenhoven, M.C.M., Gevaert, O., de Rooi, J.J., Stubbs, A.P., Duijm, J.E., Daemen, A., Bleeker, F.E., Bralten, L.B.C., Kloosterhof, N.K., et al. (2009). Intrinsic gene expression profiles of gliomas are a better predictor of survival than histology. Cancer Res. *69*, 9065–9072. https://doi.org/10.1158/0008-5472.CAN-09-2307.

78. Madhavan, S., Zenklusen, J.C., Kotliarov, Y., Sahni, H., Fine, H.A., and Buetow, K. (2009). Rembrandt: helping personalized medicine become a reality through integrative translational research. Mol. Cancer Res. *7*, 157–167. https://doi.org/10.1158/1541-7786.MCR-08-0435.

79. Bowman, R.L., Wang, Q., Carro, A., Verhaak, R.G.W., and Squatrito, M. (2017). GlioVis data portal for visualization and analysis of brain tumor expression datasets. Neuro Oncol. *19*, 139–141. https://doi.org/10.1093/neuonc/now247.

80. Cancer Genome Atlas Research Network (2008). Comprehensive genomic characterization defines human glioblastoma genes and core pathways. Nature *455*, 1061–1068. https://doi.org/10.1038/nature07385.

81. Murat, A., Migliavacca, E., Gorlia, T., Lambiv, W.L., Shay, T., Hamou, M.F., de Tribolet, N., Regli, L., Wick, W., Kouwenhoven, M.C.M., et al. (2008). Stem cell-related "self-renewal" signature and high epidermal growth factor receptor expression associated with resistance to concomitant chemoradiotherapy in glioblastoma. J. Clin. Oncol. *26*, 3015–3024. https://doi.org/10.1200/JCO.2007.15.7164.

82. Lee, Y., Scheck, A.C., Cloughesy, T.F., Lai, A., Dong, J., Farooqi, H.K., Liau, L.M., Horvath, S., Mischel, P.S., and Nelson, S.F. (2008). Gene expression analysis of glioblastomas identifies the major molecular basis for the prognostic benefit of younger age. BMC Med. Genom. *1*, 52. https://doi.org/10.1186/1755-8794-1-52.

83. Zhao, Z., Meng, F., Wang, W., Wang, Z., Zhang, C., and Jiang, T. (2017). Comprehensive RNA-seq transcriptomic profiling in the malignant progression of gliomas. Sci. Data *4*, 170024. https://doi.org/10.1038/sdata.2017.24.

84. Miller, T.E., Farran, C.A., Couturier, C.P., Chen, Z., D'Antonio, J.P., Verga, J., Villanueva, M.A., Castro, L.N.G., Tong, Y.E., Saadi, T.A., et al. (2023). Programs, Origins, and Niches of Immunomodulatory Myeloid Cells in Gliomas. Preprint at bioRxiv. https://doi.org/10.1101/2023.10.24.563466.

85. Holland, E.C. (2000). Glioblastoma multiforme: the terminator. Proc. Natl. Acad. Sci. USA *97*, 6242–6244. https://doi.org/10.1073/pnas.97.12.6242.

86. Masuda, T., Sankowski, R., Staszewski, O., and Prinz, M. (2020). Microglia Heterogeneity in the Single-Cell Era. Cell Rep. *30*, 1271–1281. https://doi.org/10.1016/j.celrep.2020.01.010.

87. Keane, L., Cheray, M., Blomgren, K., and Joseph, B. (2021). Multifaceted microglia - key players in primary brain tumour heterogeneity. Nat. Rev. Neurol. *17*, 243–259. https://doi.org/10.1038/s41582-021-00463-2.

88. Ruiz-Moreno, C., Salas, S.M., Samuelsson, E., Brandner, S., Kranendonk, M.E., Nilsson, M., and Stunnenberg, H.G. (2022). Harmonized single-cell landscape, intercellular crosstalk and tumor architecture of glioblastoma. Preprint at bioRxiv. https://doi.org/10.1101/2022.08.27.505439.

89. Bartkowiak, T., Lima, S.M., Hayes, M.J., Mistry, A.M., Brockman, A.A., Sinnaeve, J., Leelatian, N., Roe, C.E., Mobley, B.C., Chotai, S., et al. (2023). An immunosuppressed microenvironment distinguishes lateral ventricle-contacting glioblastomas. JCI Insight *8*, e160652. https://doi.org/10.1172/jci.insight.160652.

90. Sankowski, R., Böttcher, C., Masuda, T., Geirsdottir, L., Sagar, Sindram, E., Sindram, E., Seredenina, T., Muhs, A., and Scheiwe, C. (2019). Mapping microglia states in the human brain through the integration of high-dimensional techniques. Nat. Neurosci. *22*, 2098–2110. https://doi.org/10.1038/s41593-019-0532-y.

91. Zheng, G.X.Y., Terry, J.M., Belgrader, P., Ryvkin, P., Bent, Z.W., Wilson, R., Ziraldo, S.B., Wheeler, T.D., McDermott, G.P., Zhu, J., et al. (2017). Massively parallel digital transcriptional profiling of single cells. Nat. Commun. *8*, 14049. https://doi.org/10.1038/ncomms14049.

92. Frankish, A., Diekhans, M., Jungreis, I., Lagarde, J., Loveland, J.E., Mudge, J.M., Sisu, C., Wright, J.C., Armstrong, J., Barnes, I., et al. (2021). Gencode 2021. Nucleic Acids Res. *49*, D916–D923. https://doi.org/10.1093/nar/gkaa1087.

93. Hao, Y., Hao, S., Andersen-Nissen, E., Mauck, W.M., 3rd, Zheng, S., Butler, A., Lee, M.J., Wilk, A.J., Darby, C., Zager, M., et al. (2021). Integrated analysis of multimodal single-cell data. Cell *184*, 3573–3587. https://doi.org/10.1016/j.cell.2021.04.048.

94. Kowalczyk, M.S., Tirosh, I., Heckl, D., Rao, T.N., Dixit, A., Haas, B.J., Schneider, R.K., Wagers, A.J., Ebert, B.L., and Regev, A. (2015). Single-cell RNA-seq reveals changes in cell cycle and differentiation programs upon aging of hematopoietic stem cells. Genome Res. *25*, 1860–1872. https://doi.org/10.1101/gr.192237.115.

95. Germain, P.L., Lun, A., Garcia Meixide, C., Macnair, W., and Robinson, M.D. (2021). Protocol for executing and benchmarking eight computational doublet-detection methods in single-cell RNA sequencing data analysis. F1000Res. *10*, 979. https://doi.org/10.12688/f1000research.73600.2.

96. Choudhary, S., and Satija, R. (2022). Comparison and evaluation of statistical error models for scRNA-seq. Genome Biol. *23*, 27. https://doi.org/10.1186/s13059-021-02584-9.

97. Ianevski, A., Giri, A.K., and Aittokallio, T. (2022). Fully-automated and ultra-fast cell-type identification using specific marker combinations from single-cell transcriptomic data. Nat. Commun. *13*, 1246. https://doi.org/10.1038/s41467-022-28803-w.

98. Korsunsky, I., Millard, N., Fan, J., Slowikowski, K., Zhang, F., Wei, K., Baglaenko, Y., Brenner, M., Loh, P.R., and Raychaudhuri, S. (2019). Fast, sensitive and accurate integration of single-cell data with Harmony. Nat. Methods *16*, 1289–1296. https://doi.org/10.1038/s41592-019-0619-0.

99. Squair, J.W., Gautier, M., Kathe, C., Anderson, M.A., James, N.D., Hutson, T.H., Hudelle, R., Qaiser, T., Matson, K.J.E., Barraud, Q., et al. (2021). Confronting false discoveries in single-cell differential expression. Nat. Commun. *12*, 5692. https://doi.org/10.1038/s41467-021-25960-2.

100. Jin, S., Guerrero-Juarez, C.F., Zhang, L., Chang, I., Ramos, R., Kuan, C.H., Myung, P., Plikus, M.V., and Nie, Q. (2021). Inference and analysis of cell-cell communication using CellChat. Nat. Commun. *12*, 1088. https://doi.org/10.1038/s41467-021-21246-9.

101. Dimitrov, D., Türei, D., Garrido-Rodriguez, M., Burmedi, P.L., Nagai, J.S., Boys, C., Ramirez Flores, R.O., Kim, H., Szalai, B., Costa, I.G., et al. (2022). Comparison of methods and resources for cell-cell communication inference from single-cell RNA-Seq data. Nat. Commun. *13*, 3224. https://doi.org/10.1038/s41467-022-30755-0.

102. Browaeys, R., Gilis, J., Sang-Aram, C., De Bleser, P., Hoste, L., Tavernier, S., Lambrechts, D., Seurinck, R., and Saeys, Y. (2023). MultiNicheNet: a flexible framework for differential cell-cell communication analysis from multi-sample multi-condition single-cell transcriptomics data. Preprint at bioRxiv. https://doi.org/10.1101/2023.06.13.544751.

103. Yu, G., Wang, L.G., Han, Y., and He, Q.Y. (2012). clusterProfiler: an R package for comparing biological themes among gene clusters. OMICS *16*, 284–287. https://doi.org/10.1089/omi.2011.0118.

104. Palla, G., Spitzer, H., Klein, M., Fischer, D., Schaar, A.C., Kuemmerle, L.B., Rybakov, S., Ibarra, I.L., Holmberg, O., Virshup, I., et al. (2022). Squidpy: a scalable framework for spatial omics analysis. Nat. Methods *19*, 171–178. https://doi.org/10.1038/s41592-021-01358-2.

105. Erickson, A., He, M., Berglund, E., Marklund, M., Mirzazadeh, R., Schultz, N., Kvastad, L., Andersson, A., Bergenstråhle, L., Bergenstråhle, J., et al. (2022). Spatially resolved clonal copy number alterations in benign and malignant tissue. Nature *608*, 360–367. https://doi.org/10.1038/s41586-022-05023-2.

106. Kleshchevnikov, V., Shmatko, A., Dann, E., Aivazidis, A., King, H.W., Li, T., Elmentaite, R., Lomakin, A., Kedlian, V., Gayoso, A., et al. (2022). Cell2location maps fine-grained cell types in spatial transcriptomics. Nat. Biotechnol. *40*, 661–671. https://doi.org/10.1038/s41587-021-01139-4.

107. La Manno, G., Soldatov, R., Zeisel, A., Braun, E., Hochgerner, H., Petukhov, V., Lidschreiber, K., Kastriti, M.E., Lönnerberg, P., Furlan, A., et al. (2018). RNA velocity of single cells. Nature *560*, 494–498. https://doi.org/10.1038/s41586-018-0414-6.

108. Bergen, V., Lange, M., Peidli, S., Wolf, F.A., and Theis, F.J. (2020). Generalizing RNA velocity to transient cell states through dynamical modeling. Nat. Biotechnol. *38*, 1408–1414. https://doi.org/10.1038/s41587-020-0591-3.

109. Reuter, B., Fackeldey, K., and Weber, M. (2019). Generalized Markov modeling of nonreversible molecular kinetics. J. Chem. Phys. *150*, 174103. https://doi.org/10.1063/1.5064530.

110. van Dijk, D., Sharma, R., Nainys, J., Yim, K., Kathail, P., Carr, A.J., Burdziak, C., Moon, K.R., Chaffer, C.L., Pattabiraman, D., et al. (2018). Recovering Gene Interactions from Single-Cell Data Using Data Diffusion. Cell *174*, 716–729.e27. https://doi.org/10.1016/j.cell.2018.05.061.

111. Cingolani, P., Platts, A., Wang, L.L., Coon, M., Nguyen, T., Wang, L., Land, S.J., Lu, X., and Ruden, D.M. (2012). A program for annotating and predicting the effects of single nucleotide polymorphisms, SnpEff: SNPs in the genome of Drosophila melanogaster strain w1118; iso-2; iso-3. Fly *6*, 80–92. https://doi.org/10.4161/fly.19695.

112. Stummer, W., Pichlmeier, U., Meinel, T., Wiestler, O.D., Zanella, F., and Reulen, H.J.; ALA-Glioma Study Group (2006). Fluorescence-guided surgery with 5-aminolevulinic acid for resection of malignant glioma: a randomised controlled multicentre phase III trial. Lancet Oncol. *7*, 392–401. https://doi.org/10.1016/S1470-2045(06)70665-9.

113. Piccirillo, S.G.M., Dietz, S., Madhu, B., Griffiths, J., Price, S.J., Collins, V.P., and Watts, C. (2012). Fluorescence-guided surgical sampling of glioblastoma identifies phenotypically distinct tumour-initiating cell populations in the tumour mass and margin. Br. J. Cancer *107*, 462–468. https://doi.org/10.1038/bjc.2012.271.

114. Hafemeister, C., and Satija, R. (2019). Normalization and variance stabilization of single-cell RNA-seq data using regularized negative binomial regression. Genome Biol. *20*, 296. https://doi.org/10.1186/s13059-019-1874-1.

115. Reuter, B., Weber, M., Fackeldey, K., Röblitz, S., and Garcia, M.E. (2018). Generalized Markov State Modeling Method for Nonequilibrium Biomolecular Dynamics: Exemplified on Amyloid beta Conformational Dynamics Driven by an Oscillating Electric Field. J. Chem. Theor. Comput. *14*, 3579–3594. https://doi.org/10.1021/acs.jctc.8b00079.

116. Revelle, W. (2024). Psych: Procedures for Psychological, Psychometric, and Personality Research (Northwestern University). https://CRAN.R-project.org/package=psych.

117. Piccirillo, S.G.M., Reynolds, B.A., Zanetti, N., Lamorte, G., Binda, E., Broggi, G., Brem, H., Olivi, A., Dimeco, F., and Vescovi, A.L. (2006). Bone morphogenetic proteins inhibit the tumorigenic potential of human brain tumour-initiating cells. Nature *444*, 761–765. https://doi.org/10.1038/nature05349.

STAR★METHODS

KEY RESOURCES TABLE

REAGENT or RESOURCE	SOURCE	IDENTIFIER
Antibodies		
IL1RAP	Abnova	Cat# H00003556-M03; RRID: AB_489786
FZD3	Millipore Sigma	Cat# SAB4503171; RRID: AB_10761399
Alexa Fluor™ Plus 488	Thermo Fisher Scientific	Cat# A32731; RRID: AB_2633280
Alexa Fluor™ Plus 488	Thermo Fisher Scientific	Cat# A32723; RRID: AB_2633275
Biological samples		
Glioblastoma patient samples	In-house	N/A
Patient-derived cancer stem-like cells	In-house	N/A
Patient-derived tumor-associated macrophages	In-house	N/A
Chemicals, peptides, and recombinant proteins		
Neurobasal™-A Medium, minus phenol red	Thermo Fisher Scientific	Cat. No. 12349015
N2 Supplement	Thermo Fisher Scientific	Cat. No. 17502048
B-27 Supplement, minus vitamin A	Thermo Fisher Scientific	Cat. No. 12587010
human bFGF	Thermo Fisher Scientific	Cat. No. PHG0261
human EGF	Thermo Fisher Scientific	Cat. No. PHG6045
Penicillin-Streptomycin-Glutamine (100X)	Thermo Fisher Scientific	Cat. No. 10378016
CD11b MicroBeads, human and mouse	Miltenyi Biotec	Cat. No. 130-049-601
Macrophage Base Medium XF	PromoCell	Cat. No. C-28057
M2-Macrophage Generation Medium XF	PromoCell	Cat. No. C-28056
Nidanilimab (CAN04)	Selleckchem	Cat. No. A2444
Box5	Selleckchem	Cat. No. P1216
Formaldehyde	Millipore Sigma	Cat. No. FX0410-5
Triton™ X-100	Millipore Sigma	Cat. No. T8787
Goat serum	Millipore Sigma	Cat. No. G9023
Phosphate buffered saline (PBS)	Millipore Sigma	Cat. No. P2272
DAPI	Thermo Fisher Scientific	Cat. No. 62248
Recombinant Human IL-1 beta/IL-1F2 Protein	R&D Systems	Cat. No. 201-LB/CF
Corning® Matrigel® Basement Membrane Matrix, LDEV-free	Corning	Cat. No. 356234
Crystal violet	Millipore Sigma	Cat. No. 61135
Acetic acid	Millipore Sigma	Cat. No. AX0073-75
Gleolan (5-ALA)	Medexus Pharmaceuticals Inc.	N/A
Mayer's Hematoxylin Solution	Millipore Sigma	Cat. No. MHS16
Epredia™ Shandon™ Bluing Reagent	Thermo Fisher Scientific	Cat. No. 6769001
Eosin Y Solution, Alcoholic	Millipore Sigma	Cat. No. HT110116
Glycerol solution	Millipore Sigma	Cat. No. 49781
Critical commercial assays		
DNeasy Blood & Tissue Kit	QIAGEN	Cat. No. 69506
Ion AmpliSeq™ Cancer Hotspot Panel v2	Thermo Fisher Scientific	Cat. No. 4475346
Ion AmpliSeq™ Library Kit 2.0	Thermo Fisher Scientific	Cat. No. 4480441
Ion Xpress™ Barcode Adapters 1–16 Kit	Thermo Fisher Scientific	Cat. No. 4471250
AMPure XP Reagent	Beckman Coulter	Cat No. A63880
Ion 550™ Chip Kit	Thermo Fisher Scientific	Cat. No. A34537
Chromium Next GEM 3′ Single Cell Reagent kit v3.1	10x Genomics	Cat. No. PN-1000121

(Continued on next page)

Continued

REAGENT or RESOURCE	SOURCE	IDENTIFIER
Qubit dsDNA High Sensitivity (HS) assay	Thermo Fisher Scientific	Cat. No. Q32854
Human IL-1 beta/IL-1F2 DuoSet ELISA	R&D Systems	Cat. No. DY201-05
WNT5A ELISA Kit (Human)	Aviva Systems Biology	Cat. No. OKEH00723
Visium Human Transcriptome Probe Kit	10x Genomics	Cat. No. PN-1000363
NEBNext® Ultra™ II Q5® Master Mix	New England BioLabs	Cat. No. M0544
Deposited data		
snRNA-seq data	This paper	GEO: GSE259378
TCGA GBM Published dataset	Cancer Genome Atlas Research Network[80]	GEO: GSE11233
Rembrandt Published dataset	Madhavan et al.[78]	GEO: GSE68848
Gravendeel Published dataset	Gravendeel et al.[77]	GEO: GSE16011
Murat Published dataset	Murat et al.[81]	GEO: GSE7696
Lee Published dataset	Lee et al.[82]	GEO: GSE13041
CGGA Published dataset	Zhao et al.[83]	SRA: SRP027383 and SRP091303
Scripts	This paper	https://doi.org/10.5281/zenodo.14183518
Experimental models: Cell lines		
T98G	American Type Culture Collection (ATCC CRL-1690)	RRID:CVCL_0556
Human M2 Macrophages (M-CSF) monocyte-derived	PromoCell	Cat. No. C-12915
Human Microglia	Creative Bioarray	Cat. No. CSC-C1527
Software and algorithms		
Cellranger (V.7.0.0)	Zheng et al.[91]	https://www.10xgenomics.com/support/software/cell-ranger/latest
CellBender (V.0.2.0)		https://cellbender.readthedocs.io/en/latest/
Gencode Genome and Annotations	Frankish et al.[92]	hg38, gencode.v42
Seurat (V.4.3.0)	Hao et al.[93]	https://github.com/satijalab/seurat
Seurat/CellCycleScoring	Kowalczyk et al.[94]	https://github.com/satijalab/seurat
scDblFinder (V.1.12.0)	Germain et al.[95]	https://github.com/plger/scDblFinder
SCTransform (V.2)	Choudhary et al.[96]	https://github.com/satijalab/seurat
scType	Ianevski et al.[97]	https://github.com/IanevskiAleksandr/sc-type
Harmony (V.0.1.1)	Korsunsky et al.[98]	https://github.com/immunogenomics/harmony
InferCNV	Durante et al.[32]	https://github.com/broadinstitute/infercnv
SCPubr (V.2.0.1)		https://github.com/enblacar/SCpubr
LIBRA (V.1.0.0)	Squair et al.[99]	https://github.com/neurorestore/Libra
CellChat (V.1.4.0)	Jin, S et al.[100]	https://github.com/sqjin/CellChat
LIANA (V.0.1.12)	Dimitrov et al.[101]	https://github.com/saezlab/liana/
MultiNicheNet	Browaeys et al.[102]	https://github.com/saeyslab/multinichenet
clusterProfiler	Yu et al.[103]	https://github.com/YuLab-SMU/clusterProfiler
MacSpectrum (V.1.0.1)	Li et al.[47]	https://macspectrum.uconn.edu/
ShinyCellPlus		https://github.com/BioinformaticsMUSC/ShinyCellPlus
Space Ranger (V.2.0.1)		https://www.10xgenomics.com/support/software/space-ranger/latest
Squidpy (V.1.3.1)	Palla et al.[104]	https://github.com/scverse/squidpy
Seurat (spatial analysis) (V.4.9.9.9045)	Hao et al.[93]	https://github.com/satijalab/seurat
SpatialInferCNV (V.1.0.1)	Erickson et al.[105]	https://github.com/aerickso/SpatialInferCNV
Cell2Location (V.0.1.3)	Kleshchevnikov et al.[106]	https://github.com/BayraktarLab/cell2location
NCEM (V.0.1.5)	Fischer et al.[65]	https://github.com/theislab/ncem
pySCENIC (V.0.12.1)	Van de Sande et al.[37]	https://github.com/aertslab/pySCENIC

Continued

REAGENT or RESOURCE	SOURCE	IDENTIFIER
Velocyto (V.0.17.17)	La Manno et al.[107]	https://github.com/velocyto-team/velocyto.py
scVelo (V.0.2.5)	Bergen et al.[108]	https://github.com/theislab/scvelo
CellRank2 (V.2.0.2)	Weiler et al.[35]	https://github.com/theislab/cellrank
CellRank (V.1)	Lange et al.[34]	https://github.com/theislab/cellrank
GPCCA	Reuter et al.[109]	https://github.com/msmdev/pyGPCCA
MAGIC	van Dijk et al.[110]	https://github.com/KrishnaswamyLab/MAGIC
IonTorrent Alignment		https://github.com/iontorrent/TS/tree/master
Ion Torrent Variant calling		https://github.com/iontorrent/TS/tree/master
SNP EFF (V.4.3.1t)	Cingolani et al.[111]	https://github.com/pcingola/SnpEff
ZEN (blue edition)	ZEISS	N/A
GraphPad Prism (V. 10.3.1.509)	GraphPad	https://www.graphpad.com/
Other		
Qubit 2.0 Fluorometer	Thermo Fisher Scientific	Cat. No. Q32866
ZEISS Convivio microscope	ZEISS	N/A
ZEISS Blue 400 filter	ZEISS	N/A
2100 Bioanalyzer	Agilent	Cat. No. G2939BA
Ion Chef™ Instrument	Thermo Fisher Scientific	Cat. No. 4484177
Ion S5 XL System	Thermo Fisher Scientific	Cat. No. A27214
Singulomics	Singulomics Corporation (Bronx NY)	https://singulomics.com/
Chromium Controller	10x Genomics	N/A
NovaSeq 6000 Sequencing System	Illumina	Cat. No. 20012850
G4 Sequencing platform	Singular Genomics	https://singulargenomics.com/g4/
MiniMACS™ Separator	Miltenyi Biotec	Cat. No. 130-042-102
MACS® MultiStand	Miltenyi Biotec	Cat. No. 130-042-303
MS Columns	Miltenyi Biotec	Cat. No. 130-042-201
LSM 900 Confocal Microscope	ZEISS	N/A
Corning® Transwell® 6 well plates	Millipore Sigma	Cat. No. CLS3428
GlioVis data portal	Bowman et al.[79]	http://gliovis.bioinfo.cnio.es/
3D genomics	3D genomics	https://3dgeno.com/
Aperio AT2 DX System	Leica Biosystems	N/A
Arveo 8 Surgical microscope	Leica Biosystems	N/A

EXPERIMENTAL MODEL AND STUDY PARTICIPANT DETAILS

Glioblastoma patient samples

Patient informed consent was obtained through the Neurosurgery Clinics at the University of New Mexico Hospitals and at the University of Mississippi Medical Center. Tissue collection protocols were IRB-approved (Human Research Review Committee 1). Patient clinical and molecular information is provided in Table S1A.

Establishment and propagation of patient-derived cancer stem-like cells

Cancer stem-like cells (CSCs) from the tumor mass (T_Mass) and the tumor subventricular zone (T_SVZ) tissues of the patients included in this study were established as described previously[4] and propagated *in vitro* using growth factor-enriched, serum-free cell culture medium based on Neurobasal-A Medium, minus phenol red (Thermo Fisher Scientific, Cat. No. 12349015), N2 Supplement (Thermo Fisher Scientific, Cat. No. 17502048), B-27 Supplement, minus vitamin A (Thermo Fisher Scientific, Cat. No. 12587010), human bFGF (Thermo Fisher Scientific, Cat. No. PHG0261), human EGF (Thermo Fisher Scientific, Cat. No. PHG6045) and Pen/Strep/Glutamine (Thermo Fisher Scientific, Cat. No. 10378016).

Establishment of patient-derived tumor-associated macrophages

Tumor-associated macrophages (TAMs) from the T_Mass and the T_SVZ were established as described in the 'cd11b enrichment' section of the 'Method details'.

METHOD DETAILS

5-ALA administration and patient sample collection

Patients were administered with 5-Aminolevulinic acid (5-ALA) (Medexus Pharmaceuticals Inc.) 2–3 h before surgery as an oral dose of 20 mg/kg as described previously.[112,113] For detection of glioblastoma tissue, protoporphyrin IX (PpIX) was excited with blue-violet light (wavelength 375–400 nm) and fluorescence emission was read at 600–700 nm using the Arveo 8 Microscope (Leica Biosystems) or ZEISS Blue 400 filter using Convivio microscope (Zeiss). 'Fluorescence' was defined as 'visible fluorescence using the operating microscope'. Tissue was either lava orange (areas of high tumor cellularity), bleeding pink edge (infiltrating edge) or it was non-fluorescent. Tumor mass (T_Mass) and Tumor SVZ (T_SVZ) samples were defined as visibly pink/lava orange (5-ALA+) and distinguished from the non-fluorescent (5-ALA-) margin and necrotic tissue, as previously described.[4] 5-ALA+ tumor samples from the tumor mass were taken using image guidance to identify their spatial localization. 5-ALA+ SVZ samples were collected based on anatomical location with entry into the ventricular space. An approximately 5mm tissue including ventricular ependyma was collected as the SVZ sample. Physical distance from the SVZ to the tumor mass was different among patients and depended on tumor location, but in all cases, the SVZ was sampled only when fluorescence was present in the ependymal layer. Two normal SVZ (N_SVZ) samples were collected as controls from two individuals: one SVZ was collected postmortem and the other during tumor surgical resection.

Genomic DNA sequencing

Genomic DNA extraction from glioblastoma tissues was performed using the DNeasy Blood & Tissue Kit (Qiagen, Cat. No. 69506). To perform targeted gene sequencing the AmpliSeq Cancer Hotspot Panel v2 (Thermo Fisher Scientific, Cat. No. 4475346), which covers approximately 2,800 COSMIC mutations in 50 genes, was used. Libraries were prepared using Ion AmpliSeq Library Kit 2.0 (Thermo Fisher Scientific, Cat. No. 4480441) and Ion XPress Barcode Adapters (Thermo Fisher Scientific, Cat. No. 4471250) following the manufacturer's instructions. GBM samples were amplified using 10 ng of input DNA. Libraries were purified and size-selected using Agencourt AMPure XP beads (Beckman Coulter, Cat No. A63880), quantified using the Qubit 2.0 Fluorometer (Thermo Fisher Scientific, Cat. No. Q32866) and Agilent 2100 Bioanalyzer (Agilent, Cat. No. G2939BA), and diluted to 50 p.m. Diluted libraries were loaded onto Ion 550 chips using an Ion Chef instrument and sequenced on the Ion S5 XL (Thermo Fisher Scientific).

Mutation, copy-number and gene expression data

The VCF files from the Ion Torrent Variant Caller were annotated using SNP EFF v4.3.1t1. Mutations with allele frequencies below 0.05 were filtered out, as well as nonsense mutations and those with known non-pathogenic variants. For analysis of the genetic drivers for each sample, any mutations for genes *CDKN2A*, *PDGFRA*, and *TP53* were plotted in a heatmap along with gene expression and copy-number data for the same genes along with *EGFR* and *NF1*. The copy-number data were obtained from InferCNV2, averaged for each sample, and Z-scored. The gene expression data of each genetic driver were derived from the single-nucleus RNA-sequencing data, averaged for each sample, and Z-scored.

Single-nucleus RNA-sequencing

Single-nucleus RNA-sequencing and analysis were conducted by Singulomics Corporation (https://singulomics.com/, Bronx NY). In summary, frozen human tissue samples were homogenized and lysed with Triton X-100 in RNase-free water for nuclei isolation. The isolated nuclei were purified, centrifuged, and resuspended in PBS with BSA and RNase Inhibitor. The nuclei were diluted to 700 nuclei/μL and loaded to 10x Genomics Chromium Controller to encapsulate single nuclei into droplet emulsions following the manufacturer's recommendations (Pleasanton, CA, United States). Library preparation was performed according to the instructions in the Chromium Next GEM 3′ Single Cell Reagent kit v3.1. Amplified cDNAs and the libraries were measured by Qubit dsDNA HS assay (Thermo Fisher Scientific, Wilmington, DE) and quality was assessed by BioAnalyzer (Agilent Technologies, Santa Clara, CA). Libraries were sequenced on a NovaSeq 6000 instrument (Illumina, San Diego, CA, United States), and reads were subsequently processed using 10x Genomics Cell Ranger analytical pipeline and human GRCh38 reference genome with introns included in the analysis. Dataset aggregation was performed using the cellranger aggr function normalizing for the total number of confidently mapped reads across libraries. Specifically, raw base call (BCL) files were analyzed using CellRanger (v7.0.0).[91] The "mkfastq" command was used to generate FASTQ files and the "count" command was used to generate raw gene-cell expression matrices. Ambient RNA contamination was inferred and removed using CellBender (v0.2.0) with standard parameters. Human genome hg38 was used for the alignment and gencode.v42 gtf file was used for gene annotation and coordinates.[92] Data from the three areas (N_SVZ, T_SVZ, and T_Mass) were analyzed individually and subsequently integrated. Samples from patients were combined in R using the Read10X function from Seurat package(v4.3.0),[93] and an integrated Seurat object was generated. Filtering was conducted by retaining cells that had unique molecular identifiers less than 25000 and had mitochondrial content less than 5 percent. Doublets were removed using scDblFinder (v1.12.0).[95] To account for biological and technical batch differences between patients, we used SCTransform. This approach was used for count normalization, initial integration, and to identify highly variable genes.[114] We further removed batch effect between the single-cell transcriptome expression matrices of the filtered high-quality cells using Harmony (v0.1.1).[98] 3000 variable genes were selected for principal components analysis (PCA). The top 30 significant principal components (PCs) and a resolution of 0.3 for Louvain clustering were selected for Uniform Manifold Approximation and Projection (UMAP) and visualization of gene expression. Cluster markers were identified using FindAllMarkers using the Wilcoxon Rank-Sum test with

the standard parameters. N_SVZ is from two patients HNS1 and HNS2 with a total of 19988 protein coding genes and 8772 cells. T_SVZ is from 12 patients GBM7B, GBM8B, GBM9B, GBM10B, GBM12B, GBM16B, GBM17B, GBM20B, GBM22B, MIS1B, MIS2B, MIS3B with a total of 19988 genes and 37360 cells. T_Mass is from 14 patients GBM7A, GBM8A, GBM9A, GBM10A, GBM12A, GBM14A, GBM16A, GBM17A, GBM18A, GBM20A, GBM22A, MIS1A, MIS2A, MIS3A with a total of 19988 protein-coding genes and 67801 cells. For N_SVZ Cell annotation was performed using two different approaches: 1) scType, an ultrafast unsupervised method for cell type annotations,[97] and 2) Manual curation by markers to reflect the prediction results. The three areas were subsequently integrated with Harmony (v0.1.1)[98] using 30 PCA and 3000 most variable genes.

Definition of malignant cells

Putative malignant cells were identified using InferCNV analysis[32] with the following parameters - denoise TRUE, default Hidden Markov Model (HMM) settings, and a value of 0.1 for "cutoff" and the N_SVZ clusters were used are reference. Each CNV was annotated to be either a gain or a loss. Tumor cell clusters were classified based on the cell states by Neftel et al.[16] using their meta module markers and SCpubr (V2.0.1) was used to visualize the resultant enrichment. The clusters that showed an enrichment for a cell state were labeled as GBMopc (OPC-like), GBMac (AC-like), GBMmes (MES-like), GBMnpc (NPC-like), other clusters that either showed enrichment for two or more cell states or no enrichment for any cell state were labeled as GBMcc (CancerCell). Normal cells were manually curated by using canonical markers: Astrocytes - "GFAP","AQP4", Microglia - "MEF2C","P2RY12", Neurons -"SYNPR","CNR1", "SYT1", Oligodendrocytes - "MOG","MBP", OPC - "VCAN","SOX5", Endothelial - "VWF","ABCB1", Ependymal - "SPARCL1","S100B".

Cellular dynamics

Cellular dynamics were analyzed using CellRank v2.0.2[35] and CellRank v1.[34] Each area's dataset was preprocessed using the RNA Velocity steps along with gene imputation using MAGIC,[110] a required step for CellRank. This imputation step was performed using Scanpy's implementation of MAGIC. For each area (T_Mass and T_SVZ), a Velocity Kernel was computed separately for tumor and normal cells using all genes in each dataset. A GPCCA[115] estimator was used to compute macrostates, including the initial and terminal ones for each subset. The number of macrostates was determined using Cellrank's Schurr decomposition method, using an elbow plot heuristic; 5 states were selected for T_Mass normal cells, and 6 states were chosen for each of the T_Mass tumor cells, T_SVZ normal cells, and T_SVZ tumor cells. Fate probabilities were computed using the 'direct' solver with 'use_petsc' set to True. The 'ilu' preconditioner was also used in this step. This analysis produces a transition matrix, which contains the likelihood of each cell transitioning to another; this matrix is clustered to determine macrostates. From these macrostates, the one with the lowest incoming transition likelihoods is assigned as the initial macrostate. The macrostate(s) with the highest incoming or self-transition probabilities are labeled as terminal macrostates. To create heatmaps, a GAM model with 6 knots was used, and the genes selected for the heatmap correspond to the transcription factors with the top 10 regulon specificity scores per cell class.

Gene regulatory networks

Transcription factor regulatory networks were computed using pySCENIC (v0.12.1).[37] All the T_Mass samples and the T_SVZ samples were divided into sections containing only tumor and normal cells respectively, and each of these four datasets was processed separately. The gene regulatory networks were computed using the grn algorithm for each subsample. The ctx method was then run to find enriched motifs using the hg38_10kbp up/down and hg38_500bp up/down motif feather databases downloaded from https://resources.aertslab.org/cistarget/. Last, the aucell method was run to calculate regulome enrichment for each cell in each dataset. With these data, the z-scores of the cellular regulome enrichment scores were calculated and depicted in a heatmap to compare relative regulatory activity between datasets. Regulon specificity scores were calculated using the 'regulon_specificity_scores' function from pySCENIC according to the 'Cell_Class' annotations. The same method was also used for the analysis of T_Mass and T_SVZ of each individual patient.

Identification of differentially expressed genes

Genes differentially expressed were calculated between N_SVZ vs. T_SVZ, N_SVZ vs. T_Mass, and T_SVZ vs. T_Mass as a whole area. The R package LIBRA (v1.0.0) was used to perform a Wilcoxon Rank-Sum test.[99] Genes were defined as significantly differentially expressed at Benjamini–Hochberg correction FDR<0.05 and absolute value of fold change (log$_2$(Fold Change))>0.3.

Expression analysis of the SCENIC-identified ZEB1 targets

AddModuleScore() function from Seurat R package was used to find average expression levels on single-cell level for the SCENIC identified ZEB1 targets. Aggregate scores of T_SVZ and T_Mass were plotted in boxplots. Statistical significance was determined using a Wilcoxon Rank-Sum test.

Cell-cell interaction analysis

Intercellular communication network analysis was performed by using the standard workflow of the R package 'CellChat' (v1.4.0)[100] with the CellChatDB.human database to assess the primary signaling inputs and outputs. Ligand-receptor analysis framework LIANA (v0.1.12),[101] based on the consensus rank aggregate score calculated combining multiple algorithms as NATMI, iTalk, Connectome,

SingleCellSignalR, and CellphoneDB, was used to detect interactions between microglia with other tumor cells in each area. MultiNicheNet (https://github.com/saeyslab/multinichenetr) package was used to find the differences in communication of microglia cells in T_SVZ and T_Mass.

Pathway and MacSpectrum analyses

The functional annotation of the identified DEGs was performed using enrichGO from clusterProfiler R package.[103] Functional categories were selected using a hypergeometric test; categories with Benjamini-Hochberg corrected $p < 0.05$ were kept. MacSpectrum (V1.0.1)[47] a tool that uses macrophage differentiation (MDI) and polarization indexes (MPI) previously generated using *in vitro* systems was utilized to further study activation gene signatures in microglia and MDM in all three areas. To functionally characterize MDM and microglia, we used the following parameters: "pre-activation" or "M0″ cells (AMDI <0, MPI <0), "M1-transitional" (AMDI <0, MPI >0) or "M1-like" cells (AMDI >0, MPI >0), and "M2-like" cells (AMDI >0, MPI <0).

Spatial transcriptomics

Sections of formalin-fixed paraffin-embedded (FFPE) tissues of 4 GBM (GBM4, GBM7, GBM8, and GBM9, with T_Mass and T_SVZ for each) were used per 10x Genomics Visium Spatial Gene Expression for FFPE – Tissue Preparation Guide (CG000408/Rev D) as follows: FFPE blocks were first faced and scored with a scalpel blade to isolate an area of tissue up to 6 × 6 mm, then chilled on an ice block for 20 min. Paraffin sections were cut at 5 μm using a standard microtome, and floated on a 40°C waterbath, containing purified water, to remove folds and wrinkles. Sections were carefully removed from the surface of the waterbath onto a Visium Spatial Gene Expression Slide within the fiducial frames, starting with the top frame. The microtome was cleaned with xylene substitute, alcohol, and RNAse Away, and a new blade was obtained between each block. Once all frames were filled, slides were placed in a slide rack in an oven at 42°C for 3 h, then stored overnight at room temperature within a slide box containing a desiccant packet.

After overnight drying, slides were deparaffinized, stained with Hematoxylin and Eosin (H&E), and imaged per 10x Genomics Visium Spatial gene Expression for FFPE – Deparaffinization, H&E Staining, Imaging & Decrosslinking (CG000409/Rev C) as follows.

(i) for the slide deparaffinization, the following steps were taken: Xylene (3 changes, 5 min each), 100% ethanol (3 changes, 3 min each), 95% ethanol (2 changes, 3 min each), 85% ethanol (3 min), 70% ethanol (3 min), Purified water (1 min);

(ii) for the Hematoxylin and Eosin staining the following steps were taken: Mayers Hematoxylin (Millipore Sigma MHS16) – 3 min, Rinse in purified water (2 changes, 20 s and 10 s), Bluing Buffer (Fisher Scientific 6769001) – 1 min, Rinse in purified water (5 dips plus 20 s), Alcoholic Eosin (Millipore Sigma HT110116) – 1 min, Rinse in purified water (5 dips plus 20 s). Slides were then coverslipped using 85% glycerol (Millipore Sigma 49781) and immediately imaged at 20X using the Leica Aperio AT2 slide digitizing system. Coverslips were removed and slides were carefully rinsed in purified water and allowed to air dry. Decrosslinking was performed with 0.1N HCl and TE Buffer (pH 9.0) to release RNA sequestered by formalin. Pairs of human transcriptome probes (10x Genomics, PN-1000363) were hybridized to the RNA for 20 h, and libraries were prepared following the manufacturer's instructions (CG000407 Rev D). Libraries were sequenced on a Singular Genomics G4 following PCR to add G4-specific adapters. The PCR used 2 ng of library, 0.3 μM of each primer, and NEBNext Ultra II Q5 Master Mix (New England BioLabs, Cat. No. M0544) incubated at 98°C for 2 min followed by 7 cycles of 98°C for 20 s, 57°C for 30 s, and 72°C for 30 s, with a final extension at 72°C for 1 min. A similar protocol was used by 3D Genomics (https://3dgeno.com/) for the HNS1 sample (one of the two N_SVZ samples included in this study).

10x Genomics Visium analysis

Spatial transcriptomic data from the 4 GBM (GBM4, GBM7, GBM8, and GBM9) and from HNS1 were processed from FASTQ files and slides using 10x Genomics Space Ranger (v2.0.1). The GRCh38-2020-A reference transcriptome and the Human Transcriptome v1 Probe Set were used for alignment. Spatial data was then processed and visualized using Squidpy (v1.3.1)[104] for Python-based analyses and Seurat (v4.9.9.9045)[93] for R-based analyses. Downstream analysis was performed primarily in Python. Mitochondrial genes were filtered out, and SCTransform (v2)[96] was used to correct the raw counts using Analytic Pearson Residuals. Mitochondrial genes were also filtered out prior to downstream analysis.

Definition of malignant spot

Spatial copy-number variation analysis was performed using the R packages SpatialInferCNV (v1.0.1)[105] and InferCNV (v1.16.0) (https://github.com/broadinstitute/inferCNV). For each spot in each dataset, the raw gene expression counts were compiled and annotated by sample and tumor status. The N_SVZ data were used as a reference. The following parameters were used to generate the copy-number variation heatmaps: cutoff = 0.1, denoise = TRUE, HMM = FALSE.

10x Visium spot deconvolution

For cellular deconvolution, Cell2Location (v0.1.3)[106] was used on all samples to determine the cell type abundances within each Visium spot. The number of cells within each spot was determined using Squidpy, and the average value was provided as a parameter to Cell2Location in order to perform deconvolution. Cell2Location was used to filter genes using the filter_genes function with the default parameters (cell_count_cutoff = 5, cell_percentage_cutoff = 0.03, nonz_mean_cutoff = 1.12), resulting in quantities between

11,017 and 13,220 genes per dataset. We used Cell2Location's RegressionModel to help map a posterior distribution of the estimated cell type abundance for each Cell Class in the single-cell data. This model was trained for 500 epochs. With the estimated cell-type abundances, a full Cell2Location model was trained for 30,000 epochs on the spatial data to estimate the deconvolved cell types in each Visium spot. For visualizations, Cell2Location's plot_spatial function was used for each slide.

10x Genomics Visium sample clustering
Spatial data were clustered using Seurat (v4.9.9.9045)[93] using the Leiden algorithm. Cluster markers were determined using a Wilcoxon Rank-Sum Test via Seurat's FindAllMarkers function.

10x Genomics Visium spot clustering and intracellular communication
The cell type proportion of each sample were computed using the cell type abundance figures from Cell2Location (v0.1.3).[106] For each sample, the cell type abundance per spot was averaged and normalized, giving an overall cell type proportion for the entire sample. Non-negative matrix factorization was computed using Cell2Location to highlight cellular compartments. The run_colocation algorithm was run with default parameters, with the exception of n_fact, which was set to between 5 and 30 to explore a wide range of factors. The output data was reassembled into new plots to remove factors with no data. Cell2Location was used to identify cell-type specific expression of all genes in the datasets as a prerequisite for Node-Centric Expression Models. The Python library NCEM (v0.1.5)[65] was used to infer cell-cell interaction and produce visualizations. In the network plots, edges are only plotted between sender and receiver cell types that share more than 150 differentially expressed genes. Edge thicknesses are proportional to the L1 norm of the vector of fold changes.

10x Visium microglia spatial correlation
The celltype abundance values for each spot calculated by Cell2Location were used for spatial correlation analysis between microglia and other cell classes. This analysis was performed on the T_Mass and T_SVZ samples for each of the four patients with spatial transcriptomic data. The Pearson's correlation coefficients between each pair of samples were compared using an r test in the R package psych (v2.4.6).[116] A Fisher transformation was used on each correlation in order to compare them using a two-tailed t test. Statistical significance was determined with $p < 0.05$.

CD11b enrichment
Starting from briefly cultured cells obtained from the T_Mass and the T_SVZ of 4 patients (GBM 4, 7, 17, and 23) included in this study, immunomagnetic microbeads decorated with recombinantly engineered antibody fragments for CD11b (Miltenyi Biotec, Cat. No. 130-049-601) were used with the MiniMACS Separation Unit (Miltenyi Biotec, Cat. No. 130-042-102), MACS MultiStand (Miltenyi Biotec, Cat. No. 130-042-303) and MS Columns (Miltenyi Biotec, Cat. No. 130-042-201) to enrich for the CD11b+ cell fraction and establish TAMs. Specifically, cell numbers were counted and incubated with CD11b microbeads for 15 min at 4°C. Following centrifugation and resuspension, cells were run through the columns using the separation unit. Upon immunomagnetic separation, CD11b-enriched cells were plated at approximately 10^4 cells/cm^2 in M2-Macrophage Generation Medium XF (PromoCell, Cat. No. C-28056) prepared and supplemented with cytokines and mix as per the manufacturer's instructions.

IL-1β and Wnt-5a ELISA
Cell culture supernatants of 3×10^4 cd11b-enriched TAMs isolated from the T_Mass and the T_SVZ of the 4 patients (GBM4, 7, 17, and 23) and propagated *in vitro* using the M2-Macrophage Generation Medium XF (PromoCell, Cat. No. C-28056) were collected 48 h after cell passaging or after 48 h from treatment start and stored at −80°C until the assay was performed. The Human IL-1 beta/IL-1F2 DuoSet ELISA 96-wells (R&D Systems, Cat. No. DY201-05) and the Wnt-5a ELISA kit (Human): 96 wells (Aviva Systems Biology, Cat. No. OKEH00723) were used as per the manufacturer's recommendation. The experiments were performed in triplicates and repeated three times. IL-1β and Wnt-5a ELISA were also performed on TAMs following treatment with Nidanilimab or Box5. Specifically, TAMs isolated from 2 patients (GBM4, and 7 with the T_Mass and the T_SVZ for each) were treated with the IL-1RAcP fully humanized monoclonal antibody Nidanilimab (Selleckchem, Cat. No. 300113) at 20 μg/mL or with the Wnt-5a antagonist Box5 (Selleckchem, Cat. No. P1216) at 100 μM for 48 h. A total of 3×10^4 TAMs were plated in triplicate per treatment condition and were treated for 48 h with Nidanilimab or Box5 starting the day after plating. Control wells for each condition (patient and area) were also included in triplicate and the experiment was repeated three times. Cell culture supernatants were collected for ELISA.

IL-1RAcP and Frizzled-3 immunofluorescence
CSCs were plated onto glass coverslips coated with Matrigel (Fisher Scientific, Cat. No. CB-40234A) overnight. Cells were washed and fixed in 4% Formaldehyde (Millipore Sigma, Cat. No. M2-01-04) for 10 min at room temperature following permeabilization with 0.02% Triton X-100 (Millipore Sigma, Cat. No. T8787). After 1 h of blocking with 5% goat serum (Millipore Sigma, Cat. No. G9023), cells were processed for immunofluorescence using an IL-1RAcP monoclonal antibody (Abnova, Cat. No. H00003556-M03) and the FZD3 polyclonal antibody (Millipore Sigma, Cat. No. SAB4503171) at the recommended dilution of 1:200 at 4°C overnight. The next day, cells were washed with 1X phosphate buffer saline (PBS) (Millipore Sigma, Cat. No. P2272) and incubated for 1 h at room temperature with Alexa Fluor488 (Thermo Fisher Scientific, Cat. No. A32731 and A32723) used at 1:500. Cells were then counterstained

with DAPI (Thermo Fisher Scientific, Cat. No. 62248) used at 0.5 μg/mL for 10 min. After washing with PBS, coverslips were mounted onto microscope slides in mounting media. Slides were imaged in a ZEISS LSM 900 Confocal Microscope. To ensure signal specificity, every experiment was performed with control stainings (secondary antibodies and DAPI counterstaining only). We used these controls for our image settings. As additional control stainings, we included the GBM cell line T98G (ATCC, Cat. No. CRL-1690), and two commercial cell lines, namely monocyte-derived macrophages (PromoCell, Cat No. C-12915) and microglia (Creative Bioarray, Cat. No. CSC-C1527). The fluorescence intensity mean values were obtained using the draw spine contour tool in ZEN (blue edition). Image exporting to TIFF files was obtained using ZEN (blue edition). The same steps were performed for the IL-1RAcP immunostaining of TAMs.

In vitro treatment assay

To evaluate the efficacy of Nidanilimab, a IL-1RAcP fully humanized monoclonal antibody (Selleckchem, Cat. No. 300113), CSCs isolated from 3 patients (T_Mass and T_SVZ for each) and propagated in serum-free conditions as described above were treated with IL-1β and Nidanilimab. Briefly, IL-1β treatment was performed by adding the recombinant human IL-1β protein (R&D Systems, Cat. No. 201-LB/CF) to growth factor-enriched, serum-free cell culture medium at a final concentration of 100 ng/ml. Nidanilimab was used at 20 μg/mL. A total of 2.5×10^5 CSC were plated in triplicate per treatment condition and were treated for 48 h with IL-1β alone or with IL-1β and Nidanilimab starting the day after plating. The in vitro proliferative potential of CSCs was evaluated as previously described.[117] Non-linear regression analysis was performed to assess the proliferative potential.

To evaluate the efficacy of Box5, a Wnt-5a antagonist (Selleckchem, Cat. No. P1216), CSCs isolated from 3 patients (T_Mass and T_SVZ for each) and propagated in serum-free conditions as described above were exposed to conditioned medium of matched TAMs treated in vitro with Box5 for 48 h. Briefly, a total of 3×10^4 matched TAMs were plated in triplicate per treatment condition. Control wells for each condition (patient and area) were also included in triplicate. One day after plating, cells were treated with Box5 at 100 μM for 48 h. 1×10^4 cells/cm² CSCs plated in triplicates on transwell polycarbonate membranes with cell culture inserts (Millipore Sigma, Cat. No. CLS3428) pre-coated with Matrigel (Corning, Cat. No. 356234) diluted 1:50 in cell culture medium were exposed for 10-14 days to the conditioned medium of matched TAMs, treated and control. To quantify cell invasion, cells on the inside of the transwell membranes were removed using cotton swabs, and those invading the lower surface of the membranes were stained with 0.25% crystal violet (Millipore Sigma, Cat. No. 61135) for 10 min. After washing and drying, membranes were removed from the inserts and imaged by microscopy. Crystal violet was then eluted from the membranes by adding 500 μL of 33% v/v acetic acid (Millipore Sigma, Cat. No. AX0073-75) solution and shaking for 10 min. The eluted crystal violet was then transferred to a 96-multiwell plate (100 μL/well). Absorbance at 590 nm was measured using a plate reader. The experiment was repeated three times.

Survival analysis

The GlioVis data portal[79] was used to access The Cancer Genome Atlas GBM,[80] Murat's,[81] Lee's,[82] Rembrandt's,[78] Gravendeel's,[77] and Chinese Glioma Genome Atlas[83] datasets. Kaplan Meier survival curves were obtained by plotting the high and low IL1RAP and FZD3 expression levels and patient overall survival using the median expression as a cut-off. Only primary IDH wt and/or non-GCIMP GBM samples were used for this analysis. Log rank test was used to determine the association between IL1RAP and FZD3 expression levels with overall patient survival. Statistical analysis was performed using the GlioVis data portal.[79]

QUANTIFICATION AND STATISTICAL ANALYSIS

For single-nucleus RNA-seq analyses, median gene expression values were compared using the Wilcoxon Rank-Sum Test using the R package LIBRA (v1.0.0). Genes were defined as significantly differentially expressed (DEGs) at Benjamini–Hochberg correction FDR<0.05 and abs (log2(Fold Change))>0.3.

For the expression comparison analysis of ZEB1 target genes, the AddModuleScore() function from Seurat R package was used to find average expression levels on single-cell level for the SCENIC identified ZEB1 targets. Aggregate scores of T_SVZ and T_Mass were plotted in boxplots. Statistical significance was determined by comparing the median expression values using a Wilcoxon Rank-Sum test.

For pathway analyses, the functional annotation of the identified DEGs was performed using enrichGO from clusterProfiler R package.[103] Functional categories were selected using a hypergeometric test; categories with Benjamini-Hochberg corrected $p < 0.05$ were kept.

For 10x Genomics Visium sample clustering, spatial data were clustered using Seurat (v4.9.9.9045)[93] using the Leiden algorithm. Cluster markers were determined using a Wilcoxon Rank-Sum Test via Seurat's FindAllMarkers function.

For microglia spatial correlation, the celltype abundance values for each spot calculated by Cell2Location were used for spatial correlation analysis between microglia and other cell classes. This analysis was performed on the T_Mass and T_SVZ samples for each of the four patients with spatial transcriptomic data. The Pearson's correlation coefficients between each pair of samples were compared using an r test in the R package psych (v2.4.6). A Fisher transformation was used on each correlation in order to compare them using a two-tailed t test. Statistical significance was determined with $p < 0.05$.

For ELISA, each treatment condition and control experiments were performed in triplicates and experiments were repeated three times. Mean values for estimated IL-1β or Wnt-5a secretion were plotted as bar graphs (Figure 5D) or truncated violin plots (Figure 6A

left; Figure 6B left) along with standard error of the mean (s.e.m). Means were compared using unpaired t test for statistical significance. $p < 0.05$, and $p < 0.01$ are indicated in the figures with the *, and ** symbols, respectively.

Growth curves were generated to evaluate the *in vitro* proliferative potential of CSCs by plotting the mean estimated total cell number ±s.e.m on days 4, 8, and 12 or 5, 10, and 15 for each treatment. All experiments for controls and experimental groups were performed in triplicates. Statistical significance was evaluated by non-linear regression analysis. $p < 0.05$, $p < 0.001$, and $p < 0.0001$ are indicated in Figure 6A right with the *, ***, and **** symbols, respectively.

Cell migration was quantified by generating truncated violin plots using the mean absorbance values of crystal violet at 590 nm ± s.e.m. All experiments were performed as triplicates. Means were compared using unpaired t test for statistical significance. $p < 0.05$, $p < 0.001$, and $p < 0.0001$ are indicated in Figure 6B right with the *, ***, and **** symbols, respectively.

Fluorescence intensity mean values ±s.e.m were plotted for graphical representation of immunofluorescence results. Means were compared using unpaired t test for statistical significance. $p < 0.01$, and $p < 0.0001$ are indicated in Figures 5E and 5F with the **, and **** symbols, respectively.

Statistical analysis and graphical representation of results from *in vitro* treatments, ELISA experiments, immunofluorescence, and quantification of cell migration were performed using GraphPad Prism (V. 10.3.1.509).

For survival analysis, log rank test was used to determine the association between *IL1RAP* and *FZD3* expression levels with overall patient survival (Figures 6C and 6D). Statistical analysis was performed using the GlioVis data portal.[79] Significance was determined with $p < 0.05$.